

AN ABSTRACT OF THE THESIS OF

Ian M. Trakowski for the degree of Master of Science in Radiation Health Physics  
presented on June 6, 2018.

Title: Eye Lens Doses from Oblique Sources

Abstract approved:

---

David M. Hamby

Abstract:

Since the International Commission on Radiation Protection (ICRP) recommended a revision to the eye lens dose limits in ICRP Publication 118 (Stewart, 2012) the radiation protection community has conducted many new studies related to eye dosimetry. The recommended reduction of eye lens dose limits may result in the reduction of the whole body dose limit, which would affect all occupational workers in the nuclear science and engineering industries, therefore, further study is required. The need for further investigative research into eye dosimetry is due to the formation of radio induced cataracts and eye degradation from ionizing radiation and thus potential significant harm to workers. The aim of this study was to assess lens dose from oblique electron and photon point sources to see if a deterministic equation could be derived from observed data. Due to the behavior of electrons, a deterministic equation could not be derived. However, electron dose tables were developed for linear interpolation purposes. Photons were found to be influenced by their distance from the source similar to the

inverse square law. Since photons were distant dependent, a deterministic equation was derived.

© Copyright by Ian M. Trakowski

June 6, 2018

All Rights Reserved

Eye Lens Doses from Oblique Sources

by

Ian M. Trakowski

A Thesis

submitted to

Oregon State University

in partial fulfillment of  
the requirements for the  
degree of

Master of Science

Presented June 6, 2018

Commencement June 2018

Master of Science thesis of Ian M. Trakowski presented on June 6, 2018

APPROVED:

---

Major Professor, representing Radiation Health Physics

---

Head of the School of Nuclear Science and Engineering

---

Dean of the Graduate School

I understand that my thesis will become part of the permanent collection of Oregon State University libraries. My signature below authorizes release of my thesis to any reader upon request.

---

Ian M. Trakowski, Author

## ACKNOWLEDGEMENTS

I would like to convey my sincerest appreciation to my advisor Dr. Hamby for including me in this project and providing me supportive and constructive recommendations that allowed me to overcome any obstacles throughout this process. I would like to thank my colleagues David Boozer and Joshua Herrera for providing me with valuable insight and mentorship towards utilizing MCNP, in addition to unique perspectives on the topic of the lens of the eye.

## TABLE OF CONTENTS

	<u>Page</u>
CHAPTER 1 – INTRODUCTION .....	1
1.1 Overview .....	1
1.2 Research Objectives .....	3
CHAPTER 2 – BACKGROUND .....	4
2.1 Anatomy of the Eye.....	4
2.2 Cataract Formation.....	5
2.2 The Atom and Radioactive Transformations .....	6
2.3 Beta Transformations .....	9
2.4 Beta-Minus Transformations .....	10
2.5 Double Beta-Minus Transformation .....	14
2.6 Proton-rich Radionuclide Transformations .....	14
2.7 Positron Decay .....	15
2.8 Electron Capture.....	18
2.9 Beta Particle Interactions .....	19
2.10 Bragg Curve .....	21
2.11 Beta Dosimetry.....	22
2.12 Photon Interactions.....	23
2.13 Photoelectric Effect .....	24
2.14 Compton Scattering.....	25
2.15 Pair Production.....	27
2.16 Photon Attenuation.....	27
2.17 Photon Dosimetry.....	28
2.18 Charged Particle Equilibrium.....	29
2.19 Fractional Charged Particle Equilibrium.....	30
Chapter 3 – Materials and Methods .....	32
3.1 Software and Computing.....	32

## TABLE OF CONTENTS (Continued)

	<u>Page</u>
3.1.1 MCNP .....	32
3.1.2 Computing Demands .....	34
3.1.3 MCNP6 Plotter .....	35
3.1.4 MCNP Visual Editor .....	35
3.2 Simulation Geometry and Materials .....	36
3.2.1 Head and Eye Model .....	36
3.2.2 Geometry and Materials of the Head.....	37
3.2.3 Geometry and Materials of the Eyes .....	38
3.3 Source Definition .....	43
3.3.1 Source Definition and Biasing.....	43
3.4 MCNP6 Tallies.....	44
3.4.1 +F6 Tally for Beta Simulations .....	44
3.4.2 F5 Tally for Photon Simulations .....	45
3.4.2 Fractional CPE Evaluation .....	46
3.5 Deterministic Equation Development .....	49
3.5.2 Table Curve 2D .....	49
Chapter 4 – Results and Discussion.....	51
4.1 Beta Particles.....	51
4.2 Photons .....	56
Chapter 5 - Conclusion .....	61
References.....	64
APPENDICES .....	67
APPENDIX A: Electron Distribution Curves.....	68
APPENDIX B: Electron Energies vs. Absolute Position with Respect to X-Axis.....	70
APPENDIX C: Electron Eye Lens Dose Tables.....	72
APPENDIX D: KERMA vs. Absolute Distance .....	77
APPENDIX E: MCNP Input File for Electrons .....	81

## LIST OF FIGURES

<u>Figure</u>	<u>Page</u>
Figure 1: Anatomy of the Human Eye (Willoughby, 2010) .....	5
Figure 2: Nuclear Shell Configuration (De-shalit, 2014) .....	7
Figure 3: Electron Shell Configuration (Krane, 2012) .....	8
Figure 4: Nuclear Landscape (Martin, 2006).....	9
Figure 5: Carbon-14 decay on chart of nuclides and decay scheme (Martin, 2006) .....	12
Figure 6: Cobalt-60 Decay Scheme (Martin, 2006).....	13
Figure 7: Typical Beta Particle Energy Spectrum (Krane, 2012).....	13
Figure 8: Fluorine-18 Decay Scheme .....	16
Figure 9: Positron Decay Energy Spectrum (Krane, 2012) .....	17
Figure 10: Annihilation of Free Electron and Positron.....	17
Figure 11: Electron Capture of an Orbital Electron (Martin, 2006) .....	18
Figure 12: Potential Paths of a 1 MeV Electron in Water (Shultis, 2007).....	19
Figure 13: Bragg Peak of a Proton (Attix, 1986).....	21
Figure 14: Bragg Curve for Electrons in Water (Attix, 1986).....	22
Figure 15: Photon Interactions in the Eye Lens.....	24
Figure 16: Incident photon Energy vs. Scattering Angle (Knoll, 2000).....	26
Figure 17: Equilibrium of KERMA and Absorbed Dose (Martin, 2006).....	30
Figure 18: YZ Plane of Eye Inserted (left) XY Plane of Eye Inserted (right) .....	37
Figure 19: Equations Utilized to Construct the Eye (Nogueira, 2011).....	38
Figure 20: Equations Utilized to Construct the Lens of the Eye (Nogueira, 2011).....	39
Figure 21: YX Plane of Eye.....	40

## LIST OF FIGURES (Continued)

<u>Figure</u>	<u>Page</u>
Figure 22: Eye Validation Data .....	41
Figure 23: Absolute Distance between Source Position and Target Point .....	42
Figure 24: Illustration of 15 degree Cone for Electron Source.....	44
Figure 25: Fractional CPE Variable Considerations (Boozer, 2018) .....	47
Figure 26: Penetration Depth vs. Incident Angle (Boozer, 2018) .....	48
Figure 27: Illustration of TableCurve 2D Equation Output (TableCurve2D, 2018) .....	49
Figure 28: Position of Source Relative to Target Point .....	51
Figure 29: Y Positions of 3 MeV Electron Source .....	52
Figure 30: Maximum Range of a 0.8 MeV Electron Particle in the Eye.....	53
Figure 31: Dose from 1 MeV Electrons as Absolute Y-Distance Increases.....	55
Figure 32: KERMA vs. Absolute Distance.....	57
Figure 33: Logarithmic Scale Check of Photon Power Rule .....	58
Figure 34: KERMA vs. Absolute Distance of 3 MeV Photons .....	60

## LIST OF TABLES

<u>Table</u>	<u>Page</u>
Table 1: Composition of Eye and Material Densities (Nogueira, 2011) .....	40
Table 2: Dose Energy/Dose conversion Values.....	46
Table 3: Greatest Relative Error for Electrons .....	52
Table 4: MCNP Values Obtained for Electron Energies and Absolute Distances .....	56
Table 5: Greatest Relative Error for each Photon Simulation .....	56
Table 6: Coefficient Data Table.....	59

## LIST OF APPENDICIES

<u>Appendix</u>	<u>Page</u>
APPENDICES .....	67
APPENDIX A: Electron Distribution Curves.....	68
APPENDIX B: Electron Energies vs. Absolute Position with Respect to X-Axis.....	70
APPENDIX C: Electron Eye Lens Dose Tables.....	72
APPENDIX D: KERMA vs. Absolute Distance .....	77
APPENDIX E: MCNP Input File for Electrons .....	81

## LIST OF APPENDIX FIGURES

<u>Figure</u>	<u>Page</u>
Figure A. 1: 0.8 MeV Electron Distribution Relative to Eye Lens.....	68
Figure A. 2: 0.9 MeV Electron Distribution Relative to Eye Lens.....	68
Figure A. 3: 1 MeV Electron Distribution Relative to Eye Lens.....	69
Figure A. 4: 2 MeV Electron Distribution Relative to Eye Lens.....	69
Figure A. 5: Dose from 0.8 MeV Electrons as Absolute Y-Distance Increases.....	70
Figure A. 6: Dose from 0.9 MeV Electrons as Absolute Y-Distance Increases.....	70
Figure A. 7: Dose from 2 MeV Electrons as Absolute Y-Distance Increases.....	71
Figure A. 8: Dose from 3 MeV Electrons as Absolute Y-Distance Increases.....	71
Figure A. 9: KERMA vs. Absolute Distance for 3 MeV Photons.....	77
Figure A. 10: KERMA vs. Absolute Distance for 2 MeV Photons.....	77
Figure A. 11: KERMA vs. Absolute Distance for 1 MeV Photons.....	78
Figure A. 12: KERMA vs. Absolute Distance for 0.6 MeV Photons.....	78
Figure A. 13: KERMA vs. Absolute Distance for 0.3 MeV Photons.....	79
Figure A. 14: KERMA vs. Absolute Distance for 0.1 MeV Photons.....	79
Figure A. 15: KERMA vs. Absolute Distance for 0.05 MeV Photons.....	80

## LIST OF APPENDIX TABLES

<u>Table</u>	<u>Page</u>
Table A.1: 0.8 MeV Electron Eye Lens Dose Table .....	72
Table A. 2: 0.9 MeV Electron Eye Lens Dose Table .....	73
Table A. 3: 1 MeV Electron Eye Lens Dose Table .....	74
Table A. 4: 2 MeV Electron Eye Lens Dose Table .....	75
Table A. 5: 3 MeV Electron Eye Lens Dose Table .....	76

## DEDICATION

I would like to thank my mother and father, Sandra and Frederick Trakowski, who have been encouraging and emboldened me with the confidence I need to complete this process. Lastly, and most importantly, I would like to acknowledge my love and gratitude to my beautiful and caring wife, Heather Trakowski, who provides me with endless moral support and love.

## Eye Lens Doses from Oblique Sources

### CHAPTER 1 – INTRODUCTION

#### 1.1 Overview

Radiation induced cataracts have been an occupational health hazard in industries, which work with radioactive elements, since Wilhelm Roentgen first discovered X-rays in 1895. Occupational radiation exposure has led governmental and non-governmental organizations to assess and evaluate how much radiation exposure a human can receive without concern of carcinogenesis or deterministic effects. Recently, the ICRP has recommended that the occupational dose limit for the lens of the eye be reduced from 150 mSv annual dose to 20 mSv (Bolch, 2015). Radiation induced cataracts are considered to be a deterministic effect of exposure to ionizing radiation with a dose threshold of 2 Gy from a single exposure or larger fractionated doses of 5-8 Gy (Hall, 2012). The ICRP has indicated that the dose threshold for radiation induced cataracts is much lower at 0.5 Gy.

The ICRP recommended the original eye lens dose limit based on epidemiological studies conducted on the survivors of the atomic bombing of Hiroshima and Nagasaki. More recent studies have found evidence which indicates that radiation induced cataracts may occur at doses lower than 0.5 Gy with some studies finding there to be no indication of a threshold limit at all (Nogueira, 2011). The uncertainty of where the dose limit should be placed has resulted in the need for further evaluation of how the eye lens responds to different amounts of ionizing radiation exposure. A useful method to evaluate the dose received by the lens of the eye from various radiation exposure scenarios is by

using a Monte Carlo transport code (Nogueira, 2011). By using transport codes, a user can construct and simulate eye irradiation by various particles and energies so that an estimate of radiation dose can be obtained and assessed.

Computer transport codes can simulate the transport of many different radioactive particles, such as protons, alpha particles and other heavy charged particles, neutrons, electrons, and photons. For purposes of eye dosimetry the organ of concern is the lens of the eye, located at a depth of 0.3 cm behind the sclera (Nuclear Regulatory Commission, 2018). Occupational workers may be exposed to a variety of different particles, which deposit a dose to the lens. Not all particles will penetrate the eye to the depth of the lens. For example, alpha particles require an energy greater than 6.5 MeV to penetrate the dead-layer of skin, about 0.007 cm deep. Energies of this magnitude are much higher than what most laboratory and medical settings encounter. Since most alpha particles are unable to penetrate the eye to the depth of the lens, an assumption is made that heavier charged particles are also unable to penetrate to the lens and are not considered in this research. Since there are many laboratory and medical applications involving electrons (beta particles) and photons, the aim of this research is to focus on monoenergetic electrons and photons.

## 1.2 Research Objectives

The objectives of this research are: 1) to investigate how distance, incident angle, particle type, and energy effect the radiation dose to the lens of the eye; and 2) to use the data obtained from this research to develop a deterministic model which can be used to assess the dose to the lens of the eye for various exposure scenarios.

## CHAPTER 2 – BACKGROUND

### 2.1 Anatomy of the Eye

The eye is a complex organ and is sensitive to ionizing radiation (Behrens, 2011). The eye primarily consists of three different regions: the outer region, the middle layer, and the inner layer. The outer region consists of the sclera and cornea. The cornea refracts light to the retina and lens, along with protecting the eye from structural damage or infection. The sclera maintains the shape of the eye and protects the eye from external and internal forces. The middle layer consists of the iris, choroid, and ciliary body. The iris is in control of the pupil, regulating the amount of light that reaches the retina. The choroid provides nutrients and oxygen to the outer layers of the retina. The ciliary body is in control of the shape of the eye lens. The inner layer contains the retina, which is a complex structure of neurons that captures and processes the light entering the eye. The lens, located in the inner layer of the eye, changes the focal distance of the eye and the images formed on the retina (Willoughby, 2010). Figure 1 is a representation of the eye.

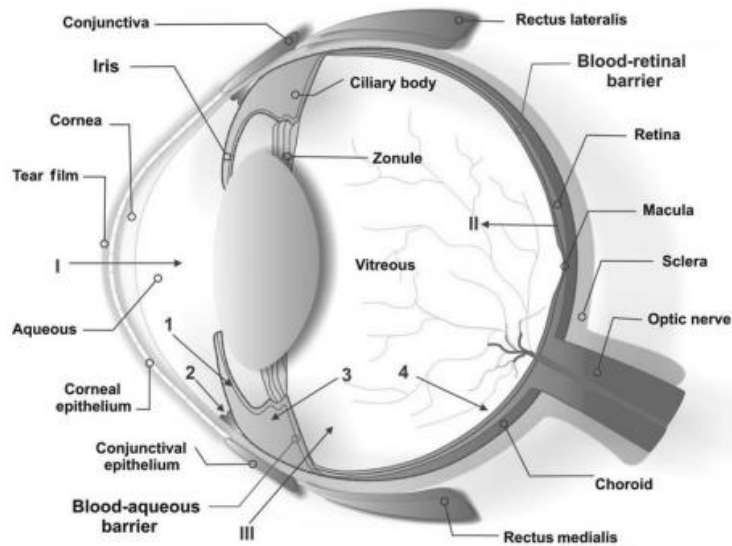


Figure 1: Anatomy of the Human Eye (Willoughby, 2010)

The lens of the eye is optically clear and, unlike other tissues, the lens is avascular and receives nourishment from the aqueous and vitreous fluids that surround it. The lens has a single epithelial cell layer, which faces the cornea and contains the underlying lens fibre cells. The transparency of the lens is dependent upon the differentiation of the fibre cells from the epithelial cells on the lens surface. The epithelial cells in the lens form and divide in the germinative zone of the eye. Once cell division and differentiation occurs the cells mature into lens fibre cells. Lens fibre cells do not contain mitochondria or nuclei and depend on the epithelial cell layer for energy production, nutrient support, and protection from harmful agents. If radiation bombardment occurs and disrupts the integrity of the lens's epithelial cell layer, cataract formation may occur (Stewart, 2012).

## 2.2 Cataract Formation

Cataract is a term which is used to describe the advanced stages of opacification in the lens of the eye. A cataract occurs in three predominant ways, which depend on

their anatomical location in the lens. The three forms of cataract formation are cortical, nuclear, and posterior capsular. Cortical cataract formation involves the more recently formed lens fibres in the outer portions of the lens found in the germinative zone. Nuclear cataract formation develops in the inner lens fibres. Posterior capsular cataracts form in the transitional zone epithelial cells and result in posterior pole opacification. Cataracts are the leading cause of blindness in the world and will occur from ocular radiation exposure (Stewart, 2012). Recent studies have shown that cataract formation has occurred at radiation doses lower than the assumed thresholds. Since many occupations in the medical, scientific, and engineering communities receive ocular exposure to ionizing radiation in the work environment further research must be performed and assessed to develop a means to reduce cataract formation. A beneficial means to evaluate ocular occupational radiation exposure would be the development of a deterministic model which may be used to assess ocular radiation dose from electron and photon radiation.

## 2.2 The Atom and Radioactive Transformations

The atom is a fundamental component of matter and is composed of subatomic particles, such as neutrons, protons, and electrons (Shultis, 2007). Atoms are commonly viewed as a “planetary” structure, which consist of a nucleus composed of neutrons and protons, surrounded by orbiting electrons. This structure is referred to as the Bohr-Rutherford model (Krane, 2012). Each atom can be uniquely identified by the number of protons,  $Z$ , and neutrons,  $N$ , that are in its nucleus. The number of protons dictates the atom’s atomic number and all atoms of the same element have the same atomic number

(Shultis, 2007). If atoms are of the same element but have a different number of neutrons in their nucleus they are referred to as isotopes of one another (Shultis, 2007).

Similar to the term isotope, the term nuclide can almost be used interchangeably with isotope to describe the constituents of atomic nuclei. The term “nuclide” is used to describe the nucleus of a particular atom based off of the specific number of protons and neutrons. Nuclides are either stable, which means they will remain the same unless perturbed, or unstable (radioactive) and will spontaneously change (Shultis, 2007). The proton, neutron, and electron configurations are organized into their own unique shells surrounding the atom. Proton and neutron shells are independent of each other, but have the same shell model applied to their configuration. If there is an imbalance of protons, neutrons, and, in some instances, electrons, within an atom a phenomenon known as atomic transition will occur in order to return the atom to a more stable or lower energy state (Krane, 2012). Figures 2 and 3 represent the nuclear and atomic shells of protons/neutrons and electrons, respectively.

Shell no.	1	2	3	4	5
s.p. states	$1s_{1/2}$	$1p_{3/2}, 1p_{1/2}$	$1d_{5/2}, 2s_{1/2}, 1d_{3/2}$	$1f_{7/2}$	$2p_{3/2}, 1f_{5/2}, 2p_{1/2}, 1g_{9/2}$
Magic no.	2	8	20	28	50
Shell no.	6			7	
s.p. states	$2d_{5/2}, 1g_{7/2}, 3s_{1/2}, 2d_{3/2}, 1h_{11/2}$			$1h_{9/2}, 2f_{7/2}, 3p_{3/2}, 2f_{5/2}, 3p_{1/2}, 1i_{13/2}$	
Magic no.	82			126	

Figure 2: Nuclear Shell Configuration (De-shalit, 2014)

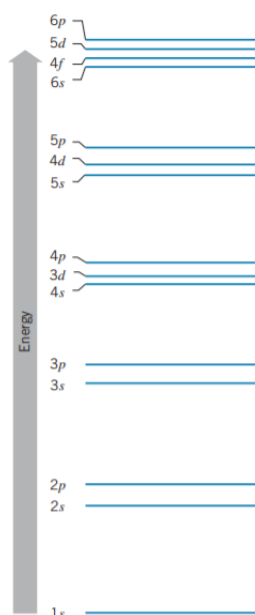


Figure 3: Electron Shell Configuration (Krane, 2012)

There are approximately 3200 known nuclides and of these, 266 are considered to be stable. Lighter stable nuclides considered have nearly equal numbers of protons and neutrons in their nucleus. When the number of protons in a nucleus increases the repulsive electromagnetic forces that might cause the nucleus to fragment will also increase (Shultis, 2007). Neutrons are needed to provide short-ranged attractive forces, known as nuclear forces, which bind the protons and neutrons (nucleons) together. Beyond an atomic number of 83 the nuclear force neutrons provide is insufficient to maintain a stable nucleus and these nuclides tend to be radioactive (Shultis, 2007). Atoms prefer to reach their most stable state if there is an excess of protons or neutrons and will begin to decay. Nuclear transformations will occur and the type of nuclear transition is heavily dependent upon whether the atom has an excess of neutrons, protons, or it is too heavy to maintain itself. Figure 4 depicts the stable nuclides in bold and radionuclides

located above the bold line are proton-rich and radionuclides below the bold line are neutron-rich.

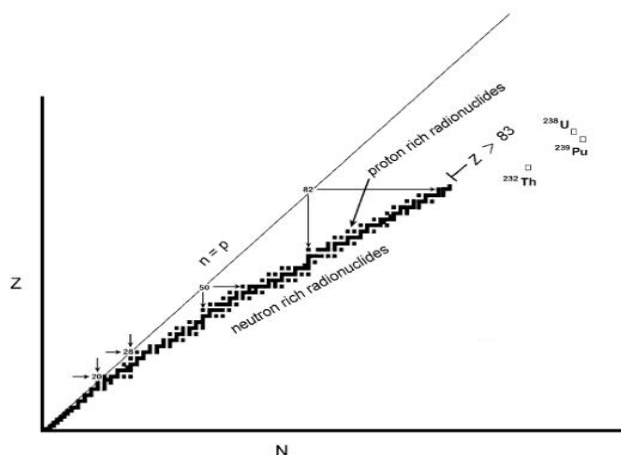


Figure 4: Nuclear Landscape (Martin, 2006)

Nuclear and atomic transitions both result in the spontaneous release of energy and are frequently referred to as radioactive decay. These transitions may either occur independently of each other or in the case of nuclear transitions can sometimes include atomic transitions as part of the radioactive decay process. There are many different methods and variations of radioactive transitions and the following sections will discuss applicable energy-loss mechanisms in detail such as beta decays and photon emissions.

### 2.3 Beta Transformations

Radionuclides with excess protons or neutrons may undergo beta decay depending on which nucleon is more abundant. This process occurs by the spontaneous change of a neutron into a proton or proton into a neutron (Krane, 2012). Since nucleons are bound together by an exact amount of energy when these atoms become unstable and spontaneously decay there is an excess energy released from the decay in addition to the

decay products. This excess energy value is known as the Q-value, which is the amount of energy gained by an atom due to a change in their bound state or the minimum energy needed to break a bound system apart (Martin, 2006). The decay products released from neutron- or proton-rich atoms may be in one of several forms: beta-minus ( $\beta^-$ ), double-beta minus ( $\beta^-\beta^-$ ), beta-plus ( $\beta^+$ ) also known as a positron decay, electron capture, double electron capture, and internal conversion. Additionally, the decay particles are accompanied by a third decay product known as a neutrino or antineutrino depending on the method of beta decay. The purpose of the neutrino is to account for the spin of the neutron or proton, which conserves momentum, energy, and charge (Krane, 2012).

#### 2.4 Beta-Minus Transformations

Neutron-rich atoms located below the line of stability on the graph of the nuclear landscape will undergo nuclear transitions such as beta-minus and double-beta minus transitions. A typical beta minus process can be observed in equation 2.1:



Here, a nucleus becomes stable by reducing its number of neutrons (n). The increase in charge occurs due to the excess energy the nuclei have, which requires a transformation process in the form of emitting a negatively charged electron ( $e^-$ ) and an antineutrino ( $\bar{\nu}$ ). The emitted electron is also more commonly referred to as a beta particle. The result of the beta transformation is an increased charge within the nucleus of the atom that emitted the beta particle in the form of a proton (p), in addition to a reduction of mass. The mass reduction of the nucleus is equivalent to the amount of the emitted energy from

the nucleus and the mass of the emitted electron (Martin, 2006). Although the mass change of the nucleus that undergoes a beta minus decay is small the energy at which the electron is emitted is quite high.

One of the most common examples of beta-minus decay process can be observed by the decay of carbon-14, which is a naturally occurring radioactive isotope of carbon. The reaction associated with the carbon-14 decay is illustrated in equation 2.2:



Here, carbon-14 decays into nitrogen-14 and emits a beta particle, an antineutrino, and the additional energy denoted by Q. The value of Q is positive, which symbolizes a spontaneous transformation. The energy from the beta decay transformation is divided between the nucleus of the recoiling product, the emitted beta particle and the antineutrino. It is the emitted beta particle that has the most energy from the transformation. After the beta transformation from carbon-14 to nitrogen-14 occurs there is a change of atomic number, which increases by one and a reduction in neutron number by one, but the mass number remains unchanged. Radioactive decays can be expressed by equations, along with being displayed visually by either their shift on the chart of nuclides or in a decay scheme (Martin, 2006). Figure 5 displays carbon-14's shift within the chart of nuclides on the left and its decay scheme on the right:

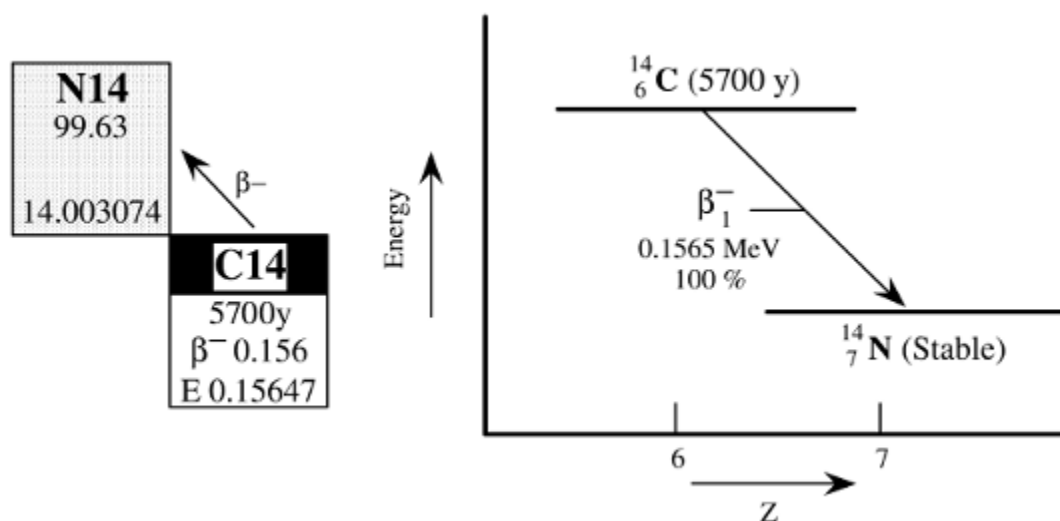


Figure 5: Carbon-14 decay on chart of nuclides and decay scheme (Martin, 2006)

Carbon-14 is an example of a radionuclide with a single beta decay, but other radionuclides may undergo much more complex beta decays. Some radionuclides like cobalt-60 and cesium-137 undergo beta transformations where there are multiple beta particles emitted with different probabilities, in addition to the potential for gamma (photon) emission following one of the beta particle routes. The process of photon emission occurs from the need for the nucleus to relieve excess energy due to the neutron shell configuration within the nucleus, so that the nucleus achieves its lowest energy state. Figure 6 displays cobalt-60's decay scheme, which includes both beta decay and the emission of photons:

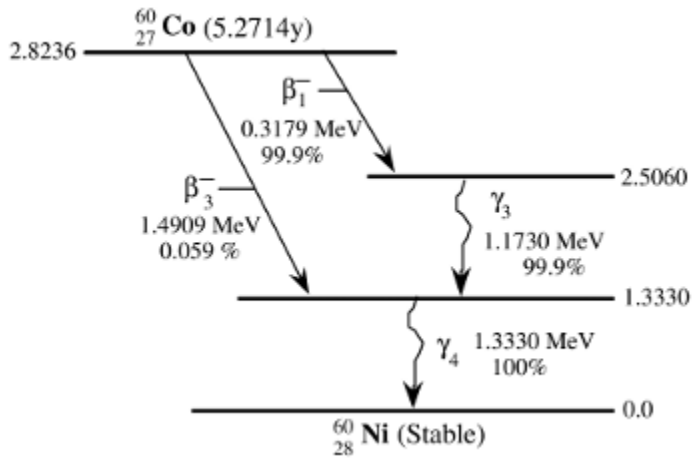


Figure 6: Cobalt-60 Decay Scheme (Martin, 2006)

Beta particles are not monoenergetic, which means that there are energy ranges associated with beta particle emission. If a less energetic beta is emitted from a nucleus there will be subsequent photon emissions from the nucleus to account for the additional energy required for the nucleus to reach its lowest potential energy (Martin, 2006). The energy ranges associated with beta particle emission form an energy spectrum. An example of a beta particle energy spectrum is shown in Figure 7:

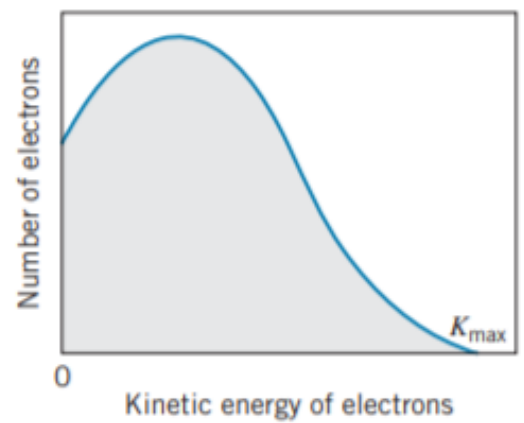


Figure 7: Typical Beta Particle Energy Spectrum (Krane, 2012)

The beta particle energy spectrum demonstrates that, if a beta that does not have the maximum beta energy is emitted from a nucleus, the conservation of energy accounts for the additional energy in the form of antineutrinos.

## 2.5 Double Beta-Minus Transformation

Both beta-minus and double beta-minus decays occur in neutron-rich radionuclides. The method in which double beta-minus decay occurs is by an unstable neutron-rich nucleus emitting two beta particles simultaneously. A double beta-minus transformation involves two neutrons spontaneously converting to two protons, along with emitting two beta particles and two antineutrinos. The end result is a nucleus with a greater binding energy, than the original nucleus. The need for the emission of two beta particles stems from the need to have a positive Q-value during a radioactive transition. In cases of double beta-minus decay a single beta decay would result in a negative Q-value, which indicates a spontaneous transformation will not occur. Radionuclides that undergo double beta-minus decay have long half-lives and these types of radioactive transformations are quite rare (Martin, 2006).

## 2.6 Proton-rich Radionuclide Transformations

Similar to beta-minus decay, proton-rich transformations occur due to instability within the nucleus. Proton-rich transformations occur in an unstable nucleus with an excess of protons. Proton-rich radionuclides are located above the line of stability on the chart of the nuclear landscape. Typically, proton-rich radionuclides are generated or produced from nuclear reactor operations and in particle accelerators (Martin, 2006). The

methods in which proton-rich radionuclides achieve stability is by either a beta plus (positron) decay or from electron capture. The end result for both of these processes is an atom that will have a proton number ( $Z$ ) one less than its parent atom (Martin, 2006).

## 2.7 Positron Decay

Positron decay is similar to beta-minus decay in the sense that there is a conversion of one nuclei to another, but the manner in which this occurs is much different than beta-minus decay. Positron decay involves a significant change in the charge of the nucleus of an atom and requires a rearrangement of the nuclei, where the nuclei become much more tightly bound. For positron decay to occur a proton within an unstable proton-rich nucleus is converted into a neutron and a positive electron, referred to as a positron. A proton has less mass than a neutron, so to account for the conservations of mass and energy the rearrangement of the atom's nuclei supplies the energy needed for the proton-to-neutron conversion and the kinetic energy needed to eject a positron.

In addition to the ejected positron, there is a subsequent electron mass, neutrino and excess energy emitted from positron decay and is illustrated by equations 2.3, 2.4, and 2.5, which illustrate the decay of fluorine-18 and the respective Q-value from the changes of mass of fluorine-18 ( $M_{F_{18}}$ ), oxygen-18 ( $M_{O_{18}}$ ), and the electron masses ( $M_{e^-}$ ):



$$Q = [(M_{F_{18}} - 9M_{e^-}) - (M_{O_{18}} - 8M_{e^-}) - M_{e^-}]c^2 \quad (2.4)$$

$$Q = [M_{F_{18}} - M_{O_{18}} - 2M_{e^-}]c^2 \quad (2.5)$$

The reason there are two electron masses is from the emission of the positron particle and the reduction in the charge of the nucleus of the oxygen-18 atom. Since there are two electron masses associated with positron decay this indicates that for positron decay to occur, there needs to be an excess amount of energy in the nucleus greater than two electron masses, which is 1.022 MeV (Martin, 2006). The maximum positron energy emitted from positron decay is equal to the difference between the energy needed to create the electron masses and the Q-value for the transformation to occur. Figure 8 illustrates the positron decay scheme associated with the decay of fluorine-18:

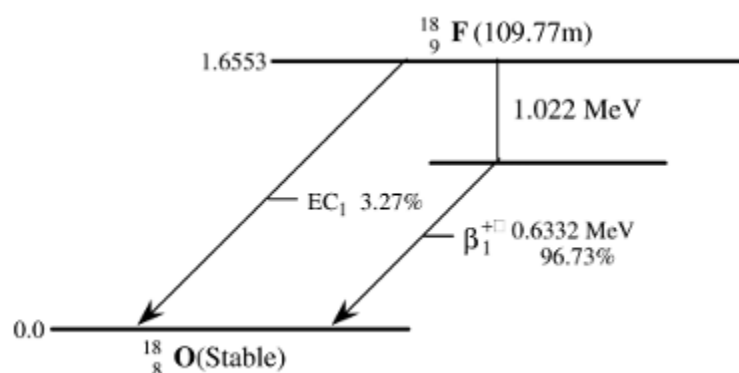


Figure 8: Fluorine-18 Decay Scheme

Like beta-minus decay, there is an energy spectrum associated with positron decay. The spectrum occurs due to the energy emitted in positron decay being shared between the positron and neutrino. Since the nucleus of an atom is positively charged and the emitted positron from a positron decay is also positively charged, the spectrum associated with positron decay is skewed to the right. Both positively charged masses naturally repel each other and the emitted positron receives an added boost when it leaves the nucleus. Figure 9 shows the spectrum for positron decay:

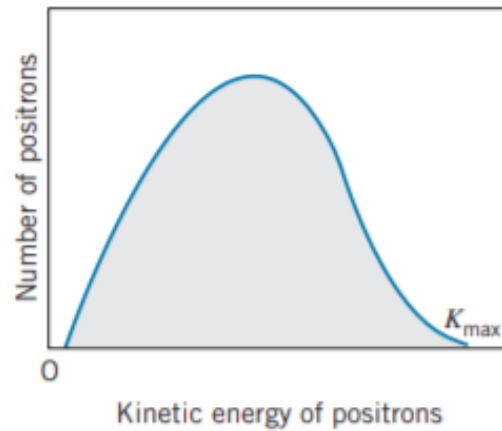


Figure 9: Positron Decay Energy Spectrum (Krane, 2012)

Positron decay involves the emission of a positively charged electron mass from the nucleus of an atom, which may also be referred to as an electron's antimatter. The antimatter emitted from positron decay will interact with free electrons that are distributed throughout all matter. When a positron and an electron interact they undergo a process called annihilation and form annihilation radiation. The annihilation radiation takes the form of two 0.511 MeV photons, which are emitted in opposite directions. Figure 10 illustrates the reaction a positron and free electron undergo when they interact with one another and annihilate:

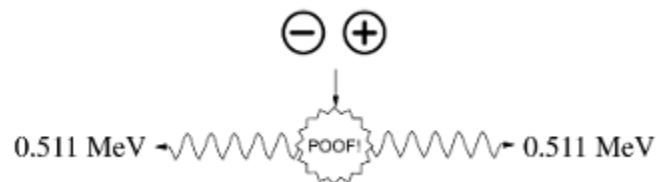


Figure 10: Annihilation of Free Electron and Positron

It is noted that the photons that are emitted from the positron annihilation reaction are not emitted from the nucleus of the decaying atom and are referred to as annihilation photons (Martin, 2006).

## 2.8 Electron Capture

Proton-rich nuclei have been noted to undergo nuclear transformations such as positron emission, but only when there is sufficient energy to emit a positron. When there is insufficient energy for proton-rich nuclei to reduce the number of protons in the nucleus by positron emission, capture of an orbital electron by the unstable nucleus will result in a reduction of the number of protons. This occurs due to the wave motion of orbital electrons near the nucleus of an atom, where an electron moves close enough to a proton-rich nucleus and is captured resulting in the reduction of the number of protons in the nucleus of an atom. Figure 11 illustrates the capture of an electron moving close enough to the nucleus of a proton-rich nucleus:

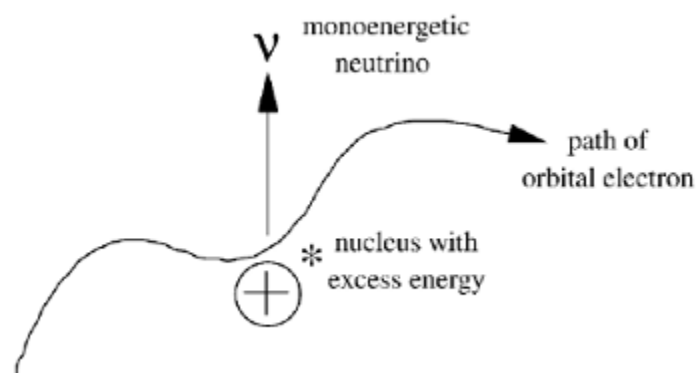


Figure 11: Electron Capture of an Orbital Electron (Martin, 2006)

The resulting reaction from electron capture is the reduction of the number of protons in a proton-rich nucleus and the emittance of a monoenergetic neutrino. Electron capture will compete with positron decay if there is sufficient energy for positron decay to occur.

Electron capture is considered to be a form of beta transformation due to the involvement of an electron, the changing of the ratio of neutrons to protons, and the mass number of an atom remaining the same after a nuclear transformation (Martin, 2006).

## 2.9 Beta Particle Interactions

Electrons and beta particles traveling through matter will interact with other electrons in the matter and scatter as they produce many ionizations. Beta particles will transfer their energy along the path they travel through matter and due to their small size will not typically travel in a straight line. Figure 12 depicts some of the paths of 1 MeV electrons as they travel through water:

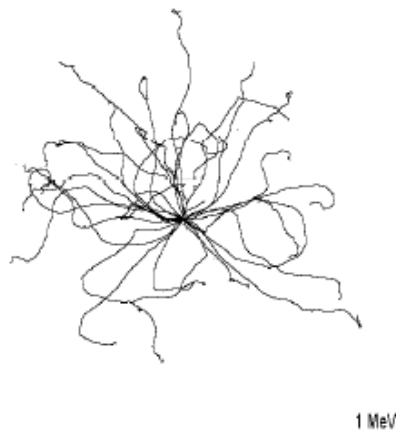


Figure 12: Potential Paths of a 1 MeV Electron in Water (Shultis, 2007)

For electrons there are two primary methods of interaction: collisional losses and radiative losses. These methods of interaction contribute to a stopping power. The term

stopping power refers to a charged particle's energy loss per unit length of distance traveled. Collisional loss contributions to stopping power are a result of the Coulombic interactions an electron experiences as it travels through a medium and interacts with other electrons. Radiative losses occur when an electron is deflected by the electric field generated by a nucleus, and bremsstrahlung radiation is produced. The fractional energy loss incurred by the electron as it travels through a medium from both collisional and radiative losses is dependent upon the energy of the electron (E) and the proton number (Z) of the material through which it travels (Shultis, 2007). The fractional energy loss of an electron from its radiative stopping power ( $S_{rad}$ ) and its collisional stopping power ( $S_{coll}$ ) is observed in equation 2.6:

$$\frac{S_{rad}}{S_{coll}} = \frac{EZ}{700} \quad (2.6)$$

Here, E is the photon energy (in MeV) and Z is the atomic number of the medium.

Similar to stopping power, another measurement of an electron's interaction in matter is an electron's linear energy transfer (LET). LET is imparted energy to a medium (Martin, 2006). LET and stopping power will be equivalent for an electron as long as there is no bremsstrahlung produced by the electron. Bremsstrahlung is the slowing down of an electron, which results in an energy release in the form of a photon. Since the photon emitted in bremsstrahlung carries energy that once belonged to the slowing down electron, a divergence between values for stopping power and LET are observed (Martin, 2006).

## 2.10 Bragg Curve

Charged particles penetrating a material show a dose vs. depth distribution in the shape of a Bragg curve or peak. Heavy charged particles like alphas and protons typically show a pronounced peak towards the end of the path they travel, because they do not deposit energy evenly throughout the material they traverse. The heavy charged particles tend to deposit most of their energy towards the end of their range, before they come to rest. Unlike heavy charged particles, the small mass of electrons do not result in a Bragg peak towards the end of their projected range. Figures 13 and 14 illustrate the differences between Bragg peaks of a proton and electron, respectively:

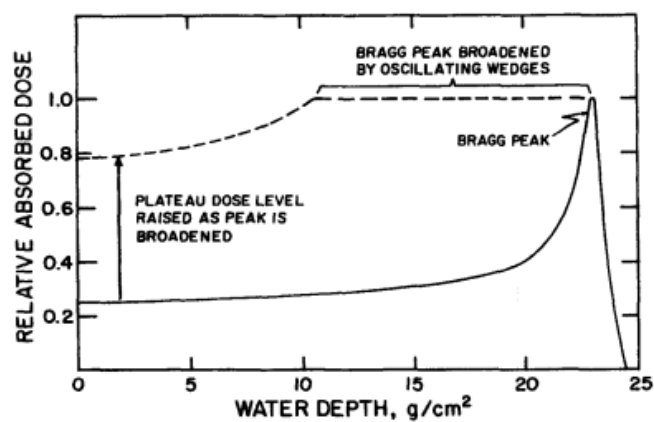


Figure 13: Bragg Peak of a Proton (Attix, 1986)

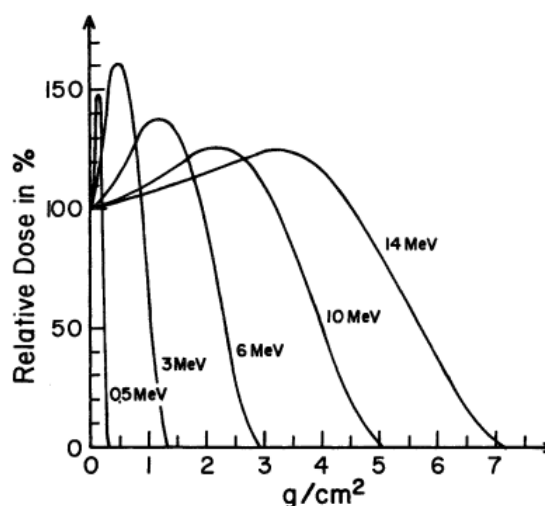


Figure 14: Bragg Curve for Electrons in Water (Attix, 1986)

The small mass of the electron causes the electron to scatter easily, which is typically due to radiative and collisional losses through the medium the electron travels. This results in the electron Bragg peak to not be as pronounced as the Bragg peaks for the heavily charged particles. In Figure 14 the Bragg peak of an electron does not become pronounced unless it is an energy of 3 MeV or less.

### 2.11 Electron Dosimetry

Electron dosimetry is performed by calculating the stopping power at the depth of interest. This method relies on numerical integration of the dose-point kernel (DPK) over the volume of the electron source and the region of interest. The region of interest in this study is the target point in the eye. Although, this method of calculating dose is faster than computer simulations, accuracy of the calculation is sacrificed (Hamby, 2014). Therefore, the preferred method of electron dosimetry is by Monte Carlo simulations. Monte Carlo simulations simulate the transport of electrons and thus provide a more

accurate dose estimate (Attix, 1986). The monoenergetic electrons in this study were simulated for energies of 0.8, 0.9, 1, 2, and 3 MeV. Almost all beta emitting radionuclides emit betas in this range (Behrens, 2009).

## 2.12 Photon Interactions

Photons, which are a form of electromagnetic radiation, ionize atoms and either eject orbital electrons or interact with the Coulombic forces of a nucleus and result in the production of an electron and positron pair. There are several different photon interactions and their probabilities of occurring are dependent upon the energy of the incident photon. Photons that exist at energies between 10 eV and 20 MeV are important for dosimetry purposes and the most significant photon interactions that occur in this energy range are the photoelectric effect, Compton scattering, and pair production. The photoelectric effect is the most probable to occur for photons at low energies, Compton scattering has the greatest probability of occurring for photons in the middle of this energy range, and lastly, pair production is most important for high-energy photons (Shultis, 2007). Figure 15 depicts photon energies against different attenuation coefficients in the lens of the eye, which elicit the different photon interactions:

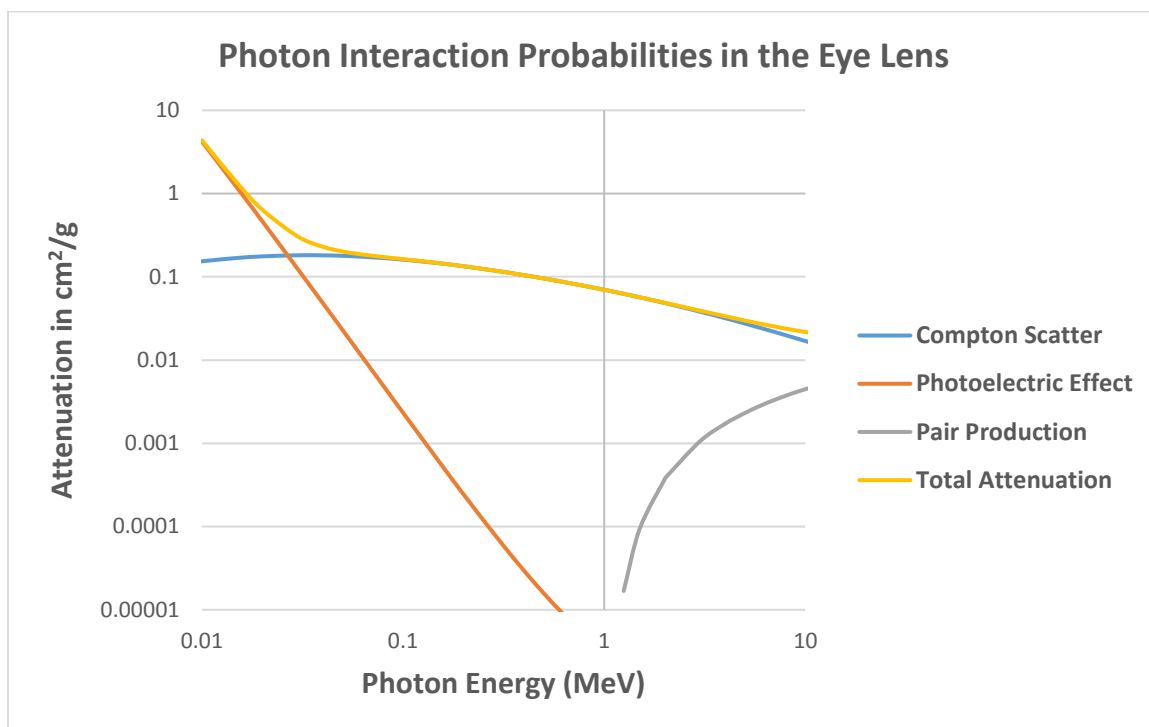


Figure 15: Photon Interactions in the Eye Lens

This study will consist of photon energies from 0.05 MeV to 3 MeV. This energy range encompasses energies considered under exposure geometries considered by the ICRP (Bolch, 2013). The energy range of photons in this study will include photons at energies of 0.05 MeV, 0.1 MeV, 0.3 MeV, 0.6 MeV, 1 MeV, 2 MeV, and 3 MeV.

### 2.13 Photoelectric Effect

The photoelectric effect occurs when a photon interacts with the electron cloud of an atom. A low energy photon will interact with an inner shell electron, which is typically an electron in the K shell of an atom. The photon will transmit all of its energy to the K shell electron and the electron will be ejected as long as the energy of the photon is greater than the electron binding energy of the K shell electron. Equation 2.7 represents

the energy of the ejected electron ( $E_e$ ), which results from the difference in energies between the incident photon ( $E$ ) and the electron binding energy ( $E_b$ ).

$$E_e = E - E_b \quad (2.7)$$

Once an orbital electron is ejected from its orbital shell, an outer shell electron will fill the vacancy and likely result in the emittance of characteristic X-rays. The energies of characteristic X-rays emitted from electron shell re-configuration are unique to each element. In some instances, instead of emitting a characteristic X-ray the energy from electronic transition is transferred to an outer shell electron and ejects the outer shell electron from its electron orbit. The ejected electron is referred to as an Auger electron (Carlson, 2013).

#### 2.14 Compton Scattering

The photon interaction known as incoherent scattering is also referred to as Compton scattering. Compton scattering occurs when an intermediate energy photon ( $h\nu$ ) imparts some of its energy to an outer shell electron, overcoming the binding energy of the outer shell electron. The result is an ejected outer shell electron ( $E_{e^-}$ ) and a scattered incident photon ( $h\nu'$ ) at an angle dependent upon the amount of energy transferred. The energies of the ejected electron and incident photon are represented in equations 2.8 and 2.9, respectively:

$$E_{e^-} = \left( \frac{\left( \frac{h\nu}{m_0c^2} \right) (1 - \cos\theta)}{1 + \left( \frac{h\nu}{m_0c^2} \right) (1 - \cos\theta)} \right) \quad (2.8)$$

$$hv' = \left( \frac{hv}{1 + \left(\frac{hv}{m_0c^2}\right)(1 - \cos\theta)} \right) \quad (2.9)$$

The quantity,  $m_0c^2$ , is the rest mass energy of an electron, which is 0.511 MeV. The incident photon has a tendency to scatter in the forward direction at higher energies, but there are two extremes associated with the scatter angle and energy transferred from the incident photon. These two extremes may occur for incident photons, which occur at angles of  $0^\circ$  and  $180^\circ$ . If there is a scattering angle of  $0^\circ$  the scattered photon has approximately the same energy as the incident photon. When a scattering angle of  $180^\circ$  occurs, maximum energy is transferred to the orbital electron. Figure 16 illustrates incident photon energy and its relation to the photon scattering angle:

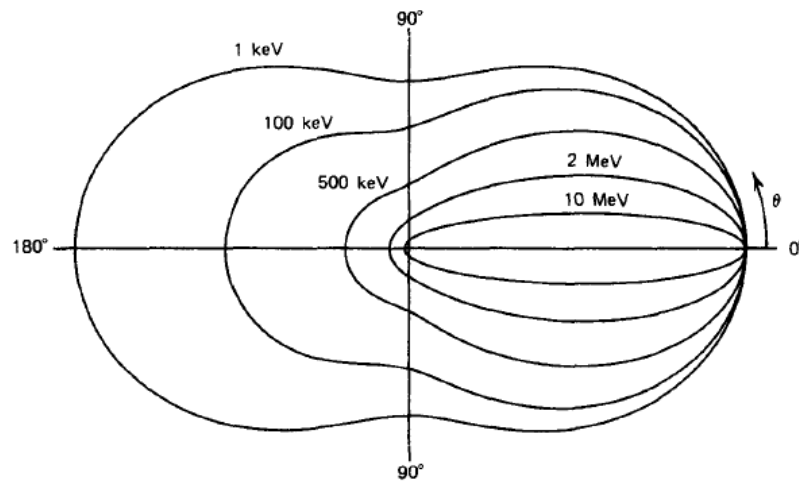


Figure 16: Incident photon Energy vs. Scattering Angle (Knoll, 2000)

### 2.15 Pair Production

The third photon interaction discussed is pair production. Pair production occurs when an incident photon with an energy equal to or greater than 1.022 MeV is completely absorbed by the Coulombic field of a nucleus. The incident photon is replaced by an electron-positron pair, which has a combined energy equivalent to the energy of the incident photon. The electron-positron pair is ejected from the atom and the electron and positron will lose their energy by energy transfer processes. Pair production is recognized by the annihilation of the positron. Positron annihilation occurs when the positron interacts with a free electron. The annihilation process results in the emittance of two 0.511 MeV photons in opposite directions (Knoll, 2000). Equation 2.10 describes how an incident photon ( $hf$ ) with an energy greater than or equal to 1.022 MeV, which is twice the rest mass of an electron ( $m_e c^2$ ), will create an electron ( $E_-$ ) and positron ( $E_+$ ) pair with energies ( $K_-$ ) and ( $K_+$ ), where  $K_-$  and  $K_+$  are positive:

$$hf = E_+ + E_- = (m_e c^2 + K_-) + (m_e c^2 + K_+) \quad (2.10)$$

### 2.16 Photon Attenuation

Photons interact with matter in different ways than charged particles. As photons or X-rays travel through a material some may pass through without an interaction, some are absorbed by the material, and some may be scattered away from the primary photon beam. A photon beam's initial intensity ( $I_0$ ) is expressed by an exponentially decreasing function with the thickness of an absorber ( $x$ ) and the linear attenuation coefficient ( $\mu$ ),

which results in the intensity of the beam after it traverses through the absorbing material ( $I$ ). Equation 2.11 illustrates the equation for photon beam intensity:

$$I = I_0 e^{-(\mu x)} \quad (2.11)$$

The linear attenuation coefficient ( $\mu$ ) is comprised of the sum of each of the principal modes of photon interactions, which are the photoelectric effect ( $\tau$ ), Compton scattering ( $\sigma$ ), and pair production ( $\kappa$ ). Equation 2.12 expresses the equation for the linear attenuation coefficient:

$$\mu = \tau + \sigma + \kappa \quad (2.12)$$

### 2.17 Photon Dosimetry

To determine how much radiation dose the lens of the eye has received from particle interactions and ionizations the concepts of absorbed dose and charged particle equilibrium must be addressed. Absorbed dose ( $D$ ) is the amount of mean energy deposited (J) by ionizing radiation per unit mass (kg) and has units of gray (Gy) (Martin, 2006). Absorbed dose is determined by the photon fluence ( $\Phi$ ), energy of the photon ( $E_\gamma$ ), and mass energy absorption coefficient ( $\frac{\mu_{en}}{\rho}$ ). Equation 2.13 depicts the method to calculate absorbed dose for photons:

$$D = \Phi E_\gamma \left( \frac{\mu_{en}}{\rho} \right) \quad (2.13)$$

Similar to photon attenuation, absorbed dose must account for various photon interactions traversing a medium like the eye. Some of the interactions that take place may produce radiative energy, which is carried out of the medium. Since there is energy loss out of the

medium the linear attenuation coefficient cannot be used to determine energy deposition (Martin, 2006). The mass energy absorption coefficient is the product of the mass energy transfer coefficient ( $\frac{\mu_{tr}}{\rho}$ ) and the fraction of energy of secondary charged particles, which are lost to bremsstrahlung in the material traversed (Shultis, 2007). The value for the mass energy absorption coefficient is dependent upon the absorption probability of the material, the density of the absorbing material, and the energy of the incident photon.

### 2.18 Charged Particle Equilibrium

To calculate absorbed dose the condition of charged particle equilibrium (CPE) must exist. For ideal cases with no attenuation, CPE is established when the kinetic energy released in matter (KERMA) is constant with depth, there are no energy losses due to bremsstrahlung, and absorbed dose is equivalent to KERMA. KERMA is a measurement of the kinetic energy per unit mass produced from indirectly ionizing radiation. KERMA (K) is dependent upon the energy of the photon ( $E_\gamma$ ), photon fluence ( $\Phi$ ), and the mass energy transfer coefficient ( $\frac{\mu_{tr}}{\rho}$ ). Equation 2.14 depicts the calculation for KERMA:

$$K = \Phi E_\gamma \left( \frac{\mu_{tr}}{\rho} \right) \quad (2.14)$$

The difference between KERMA and absorbed dose is KERMA corresponds to the transferred kinetic energy to charged particles by photon interactions while traversing an incremental distance in a material. The units of KERMA are joules per kilogram and KERMA is an approximation of dose when CPE is established. Figure 17 depicts the association of KERMA, absorbed dose, and CPE:

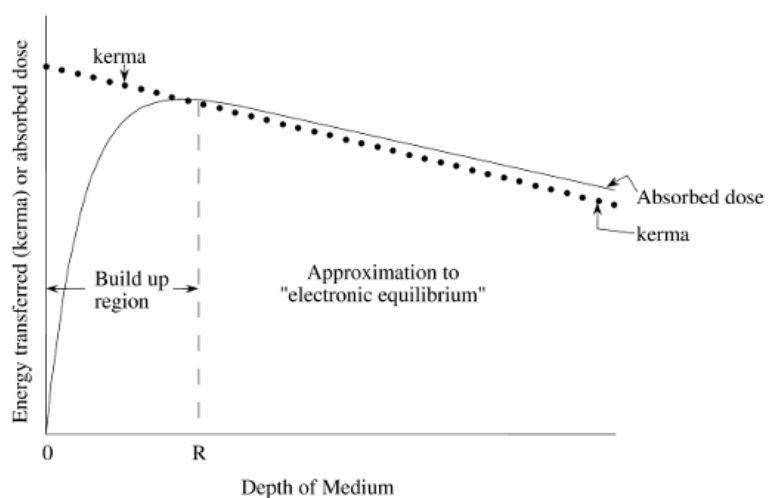


Figure 17: Equilibrium of KERMA and Absorbed Dose (Martin, 2006)

CPE is established when KERMA and dose are equal at depth  $R$ . Here, the charged particles leaving a small volume are replaced by others with the same energy, type, and direction (Shultis, 2007). The lens of the eye is at a depth of 0.3 cm and, for most photon energies of interest, is located in the buildup region where CPE does not exist.

Fortunately, Monte Carlo simulations can be utilized to assess the difference between KERMA and absorbed dose in the buildup region, where a correction factor,  $f_{CPE}$ , may be introduced to KERMA to estimate the absorbed dose in the buildup region.

### 2.19 Fractional Charged Particle Equilibrium

Monte Carlo simulations have been performed to account for the fractional charged particle equilibrium ( $f_{CPE}$ ), if CPE has not been established. This was performed by creating a cylindrical water volume with a radius of 2 cm and a photon beam source with a radius of 2 cm directed at the water volume. The cylindrical water volume with a

length of 4 cm was incrementally divided into several volumes with thicknesses of 100 microns. The Monte Carlo simulation accounted for absorbed dose and KERMA in each incremental volume. To determine,  $f_{cpe}$ , the ratio of KERMA to absorbed dose was determined for each disc. Equation 2.15 may be used to determine dose in the buildup region:

$$D = K \cdot f_{CPE} \quad (2.15)$$

## Chapter 3 – Materials and Methods

### 3.1 Software and Computing

#### 3.1.1 MCNP

The simulations orchestrated in this study were performed using the Monte Carlo N-Particle software package (MCNP), which is a Monte Carlo code developed and currently maintained by Los Alamos National Laboratory. MCNP is a general purpose, generalized-geometry, continuous-energy, time-dependent, coupled /photon/electron/neutron transport code (X-5 Monte Carlo Team, 2008). There are many transport modes that can be utilized by this software and are applicable to this study: photon only, electron only, or electron/photon. The various transport modes can be utilized to simulate the movement of particles through materials that encompass many different geometries and energies. Electron transport consists of collisional energy loss with optional energy straggling, angular scattering due to Coulombic interactions, and the production of several secondary particles like K shell electron impact ionizations, Auger electrons, knock-on electrons, which are secondary electrons produced from large-angle scattering of beta particles, and bremsstrahlung (X-5 Monte Carlo Team, 2008). For photon transport, MCNP can account for coherent and incoherent scatter, absorption via pair production, and fluorescent emission after photoelectric absorption (X-5 Monte Carlo Team, 2008). MCNP utilizes random number selection, which samples the probability distributions that govern these particle interactions. The Monte Carlo method requires the user to develop an input file, which includes a defined source, and MCNP

tracks the path of the primary and secondary particles until extinction. The particles observed by the software are tracked and then scored dependent upon user input.

The input file should consist of several different sections of defining cells, surfaces, and data used to describe a simulation. These defined items are referred to as cards. The primary items defined by an input file are the cell cards, surface cards, and data cards. Each of these cards are separated by a blank line. Cell cards require the user to enter the material number, material density and specifications used to describe the geometry of the cell (X-5 Monte Carlo Team, 2008). Surface cards use a numerical designator, surface mnemonic, and equation, which describe the surface specific orientation of an object that is used for the development of the cell cards (X-5 Monte Carlo Team, 2008). The data cards consist of individual secondary cards used to provide additional information to the MCNP program. Secondary data cards include a mode card, cell and surface parameters, source specification, tally specification, material specification, and problem cutoffs (X-5 Monte Carlo Team, 2008). The tally specification card is useful for MCNP simulation, because it allows the user to input the type of information desired from the simulation, such as estimating energy deposition or flux at a point. Before an MCNP simulation will run properly, the software performs several checks, which are used to evaluate any errors associated with the input file. If any errors are found and are considered to be “fatal errors” the simulation will cease the run and provide the user with information regarding where the errors exist in the input file.

The execution of an MCNP simulation requires the user to construct an input file with unambiguous cell, surface, and data cards. The amount of run-time an MCNP

simulation will take is dependent upon the complexity and geometry of the cells and surfaces, along with desired precision. Simulations may take minutes, hours, and even days depending upon the accuracy and number of particles the user chooses. Once the precision, number of particles, or both items have been determined and properly formatted into the input file the simulation is run and an output file is generated. The output file is quite large in comparison to the input file and consists of a substantial amount of information obtained from the simulation including the information the user desired from the tally, the tally's precision, and ten statistical checks performed by the software. The ten statistical checks are analyzed to determine whether the user defined tallies have not been sampled well. MCNP provides the user with many tally options used to obtain information like flux, current, pulse height, and energy deposition from each simulation. The output tallies can assist the user in determining radiation dose associated with various energies and materials. MCNP is a simulation software that has many different versions available, but MCNP version 6 was used for the performance of this study.

### 3.1.2 Computing Demands

MCNP version 6 (MCNP6) is capable of providing the desired output information for this study. The use of multiple cores and processors was required for the performance of MCNP6 simulations. MCNP6 allows the user to utilize all of a CPU's cores and processors. The computer specifications used for the performance of this study are 16 GB of RAM, with model 8 processors rated at 2.70 GHz per core. Unlike other earlier versions, MCNP6 allows the user to select the number of processors to use for a given simulation. The number of cores and processors utilized for simulation purposes will

tremendously decrease the amount of time the software requires to perform a simulation, allowing more histories in a shorter amount of time. MCNP6 software provided the necessary options a user can use to achieve a desired output performance.

### 3.1.3 MCNP6 Plotter

One of the more time intensive portions of this study was ensuring the operators used to define the geometry of each cell were described appropriately and did not result in fatal errors. The MCNP6 geometry plotter was used extensively throughout this study, which allows the user to visually see any geometry errors associated with an input file. When an input file is run in MCNP the user may choose to plot the input file, which will utilize the MCNP6 plotter and generate a two-dimensional representation of the input file geometry. The eye and head phantom models used in this study were plotted using the MCNP6 plotter to evaluate and correct errors observed in the input file. To utilize the MCNP6 plotter an X-windows server and MobaXterm Personal Edition v10.5 Build 3582 were used.

### 3.1.4 MCNP Visual Editor

Like MCNP6 Plotter, MCNP Visual Editor was used to evaluate the geometry of the input files. MCNP Visual Editor provides the user with the ability to manipulate two and three dimensional geometry plots associated with an input file. The MCNP Visual Editor produces multiple cross-sectional views of an input file, in addition to tracking and displaying particles associated with an MCNP simulation. Visually tracking and displaying particles is an invaluable way of ensuring the input file has been manipulated appropriately to ensure a source is defined properly and will yield the desired output.

Two-dimensional and three-dimensional plots obtained from MCNP Visual Editor included in this study are labeled accordingly.

### 3.2 Simulation Geometry and Materials

#### 3.2.1 Head and Eye Model

The head and eye models used in this study were created by the Oak Ridge National Laboratory and Nogueira (2011), respectively. The purpose of the head model was to have a head phantom with the physiological properties of a human head for MCNP simulations (Eckerman, 1996). Since dose to the lens of the eye is the main focus here, an eye that met the criteria for ICRP dose estimates was needed. The eye developed by Nogueira (2011) incorporated the dimensions and geometries of the eye noted in the works of Charles (1975), Worgul (1991), and work published in NCRP report no 130 (Nogueira, 2011). Charles and Brown published work evaluating the dimensions of the eye and the position of the lens of the eye corresponding to estimated dose (Charles, 1975). This work was later incorporated into work conducted by Behrens used for ICRP eye lens dose estimates. The work by Worgul (1991) provided mathematical equations used for the geometries of the different components of the eye (Worgul, 1991). The dimensions and geometry of the eye determined by Worgul (1991) were reported in NCRP report no 130. The purpose for utilizing Worgul's (1991) work was for the more detailed dimensions and geometry for the lens of the eye, which included the different zones of the lens including the germinative zone; the most sensitive cell population in the lens of the eye (Nogueira, 2011). For the purposes of this study the eye model developed

by Nogueira (Nogueira, 2011) has been inserted into the head phantom developed by Eckerman (Eckerman, 1996).

### 3.2.2 Geometry and Materials of the Head

The geometry and materials used in the construction of the head phantom were found in source materials from Eckerman (1996) and Krstić and Nikezić (2007). The work from Krstić and Nikezić (2007) created an MCNP input file of a human phantom that could be utilized for MCNP simulations. The human phantom consists of various portions of the human body, but most important to this study was a human head with appropriate physiological properties, shapes, and material composition. The coordinate system for the phantom model utilizes a Cartesian system, where the z-axis is vertically upward and the x and y axes are horizontal to the left and right sides of the phantom (Krstić, 2007). Figure 18 depicts the head phantom with the eyes inserted:

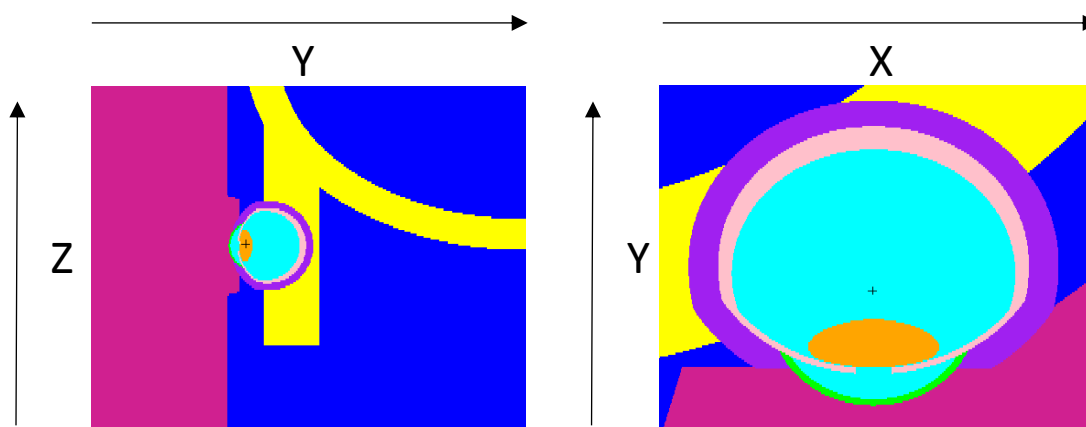


Figure 18: YZ Plane of Eye Inserted (left) XY Plane of Eye Inserted (right)

The phantom models generated by Krstić and Nikezić (2007) were compared to several other phantom models, which incorporated items from ICRP recommendations (ICRP 60, 74, 23, and 89). Phantoms were irradiated by Krstić and Nikezić (2007) using

a photon source ranging from 0.1 MeV – 10 MeV in energy to calculate their own dose conversion factors. Discrepancies were noted for photon energies lower than 1 MeV, but above 1 MeV there were differences no less than 5% when compared to ICRP 74 values (Krstić, 2007).

### 3.2.3 Geometry and Materials of the Eyes

The geometries and dimensions of the eye model utilized in this study are from research by Nogueira (2011). The eye model is quite detailed and consists of the choroid, retina, sclera, vitreous humour, cornea, anterior chamber, eye lid, and lens. Nogueira (2011) included special detail associated with the various components of the lens of the eye, including the central zone, transition zone, germinative zone, and meridional rows. Figures 19 and 20 represent the equations with units of millimeters used to construct the larger portions of the human eye and the detailed lens of the eye, respectively.

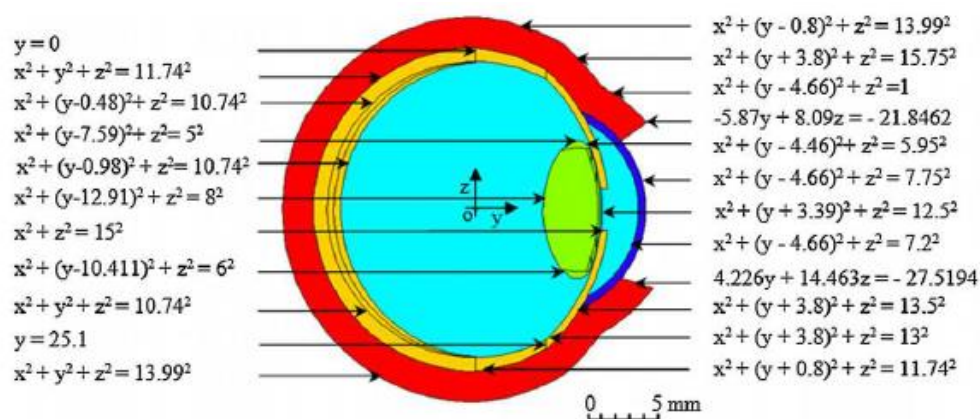


Figure 19: Equations Utilized to Construct the Eye (Nogueira, 2011)

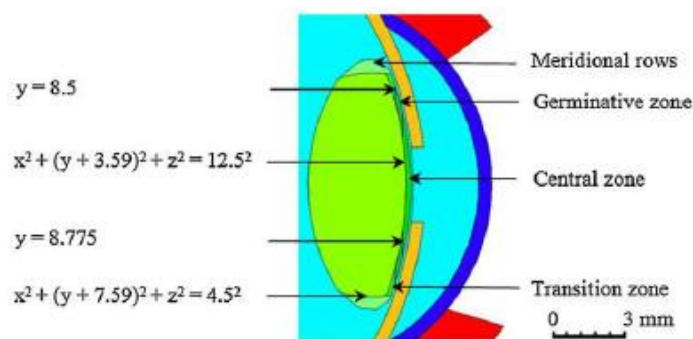


Figure 20: Equations Utilized to Construct the Lens of the Eye (Nogueira, 2011)

The model of the eye consists of 33 surfaces and 13 cells and the dimensions were modeled from the works of Charles (1975), Worgul (1991), and ICRP 89. Corrections were made to the equations in Figures 19 and 20 and are updated in the input file in Appendix E. This model of the eye has included special detail of the eye lens. The different zones within the lens of the eye consist of epithelial cells, which are formed and distributed from the germinative zone. The germinative zone is the most sensitive portion of the lens of the eye and is the primary location of the eye where cataract induction occurs (Nogueira, 2011). The elements and materials of the eye by Nogueira (2011) are illustrated in Table 1 and are color coordinated with Figure 21:

Elemental Composition (% mass)											
Region	Density	H	C	N	O	Na	P	S	Cl	K	Color
Cornea	1.06	10.3	10.9	3.5	75.1			0.2			Green
Anterior Chamber	1	11.2			88.8						Light Green
Lens	1.07	9.6	19.5	5.7	64.6	0.1	0.1	0.3	0.1		Yellow
Vitreous Humour	1.00	11.2			88.8						Light Blue
Retina and Choroid	1.07	10.0			88.8						Light Blue
Sclera	1.07	10.0	14.6	4.5	70.6			0.3			Royal Blue
Eye Lid	1.09	10.0	19.9	4.2	65.0	0.2	0.1	0.2	0.3	0.1	Dark Blue

Table 1: Composition of Eye and Material Densities (Nogueira, 2011)

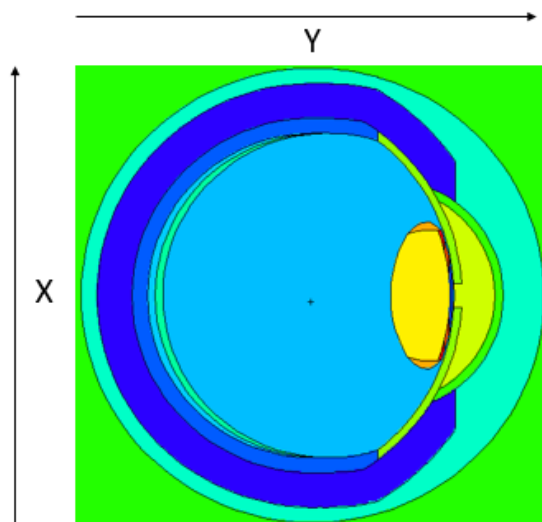


Figure 21: YX Plane of Eye

Once the eye is completed a validation process is performed to verify the eye created by the user has the same properties as the eye developed by Nogueira (2011). The eye validation is illustrated by Figure 22, which depict the results from Nogueira (2011), Behrens (2009), and this report.

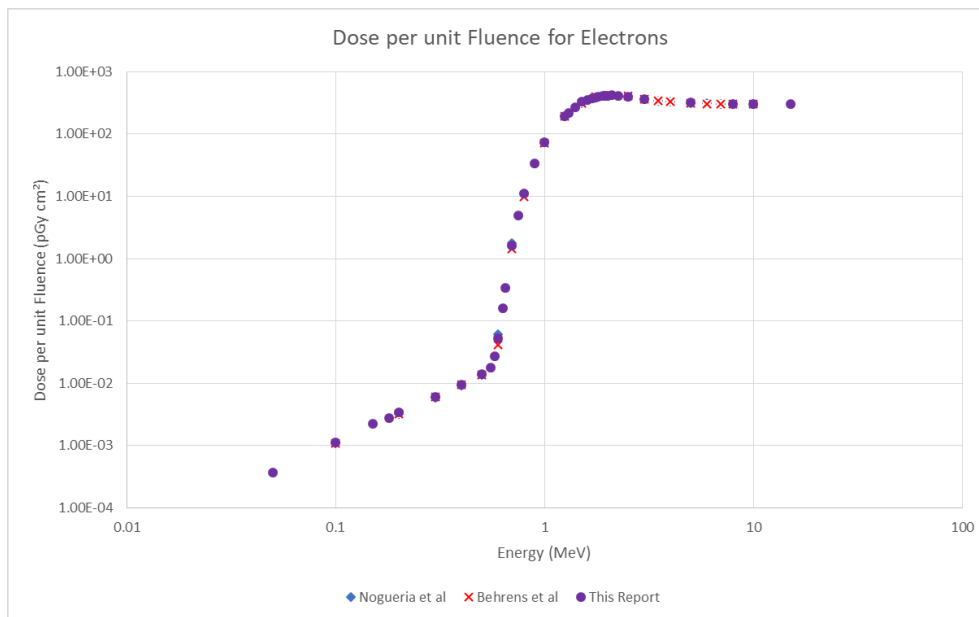


Figure 22: Eye Validation Data

### 3.2.4 Distance between Target Point to Source Point

The target point is located 0.3 cm deep into the eye. The position of the target point is considered to be the origin of this plane. For this study the source is positioned at X-coordinates from -0.5 to 0.5 cm and Y-coordinates which range from -0.359 to -0.859 cm. In this study the term “centerline” refers to the position where X equals zero. Figure 23 illustrates the positioning of the source in relation to the target point. The starting point the source is positioned is at -0.5, -0.359. The distance between the target point and the moving source is referred to as the absolute distance with units (in cm). The source is moved in 0.1 cm increments along the X-axis, crossing over the centerline position, until

it reached the position of 0.5, -0.359. The source is then moved away from the target point, along the Y-axis in -0.05 cm intervals. The next starting position of the source is -0.5, -0.409. The source is moved in this manner for several iterations and has an ending point of 0.5, -0.859. To assess how the absolute distance effects the absorbed dose from the electron and photon point sources, the X-coordinate position of the point source is held constant, denoted by the X-coordinate position in the legend for each figure for electrons, and the absolute distance is the distance between the point source and the target point for a given X-coordinate position.

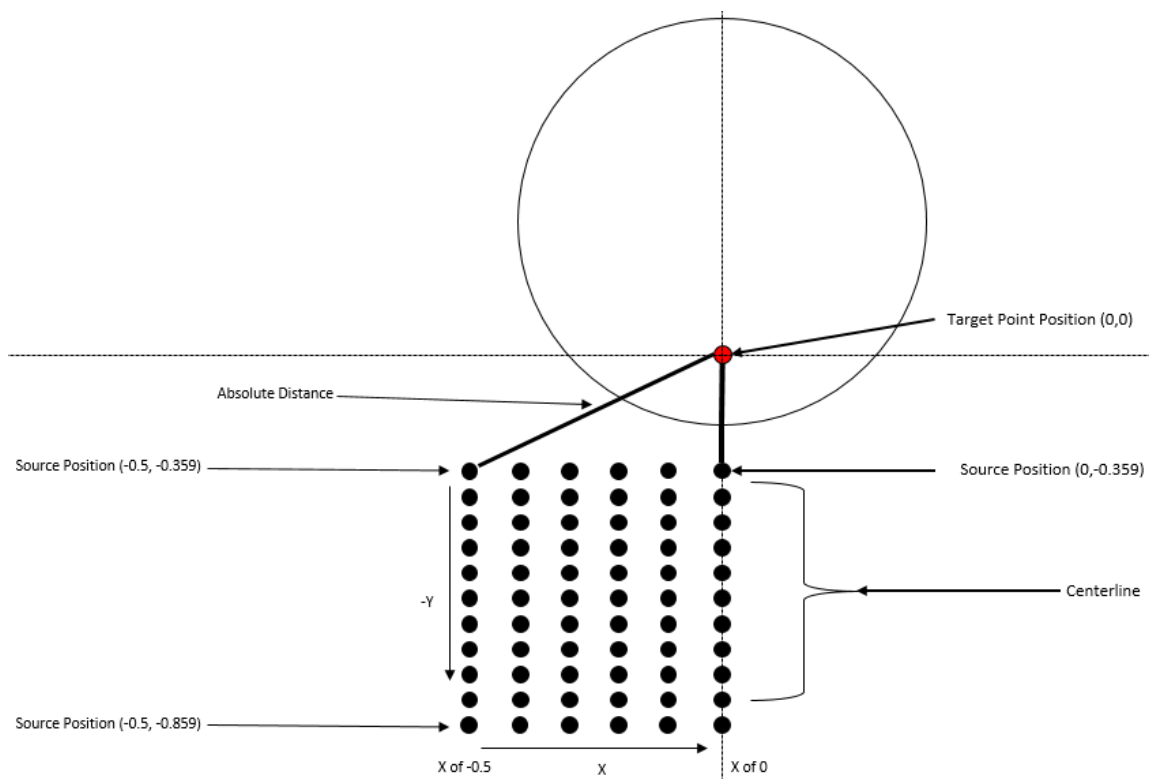


Figure 23: Absolute Distance between Source Position and Target Point

### 3.3 Source Definition

#### 3.3.1 Source Definition and Biasing

The simulations performed in this study used monoenergetic electrons and photons for all of the respective MCNP simulations. Simulations were performed at values for electrons of 0.8, 0.9, 1, 2, and 3 MeV and value for photons of 0.05, 0.1, 0.3, 0.6, 1, 2, and 3 MeV. There were a total of 121 simulations associated with each particle type, particle energy, and source position. To reduce the amount of variance associated with each simulation, variance reduction methods were incorporated into each simulation run. These techniques allow for an increase in the probability of an interaction in the cell of interest without affecting the validity of the end result.

Source biasing provides the user with the ability to modify the source direction in a way to reduce computation time so the simulation is not accounting for particles that are highly unlikely to interact with the target. This is performed by reducing the weight of the photons entering the cone of interest aimed at the target to keep the game fair. The user alters the direction of the particles emitted from an otherwise isotropic point source towards the target cell. Specific cone cosines on the source information (SI) card, biasing probabilities on the source biasing modifier (SB) card, and true distribution on the source probability (SP) card are used to keep calculations correct. The SI card takes the source definition distribution and divides it into histogram bin limits, the bin sorts the data, and the SI card has histogram bin boundaries with a bin limit range from -1 to 1 and changes with respect to  $\cos\theta$ . The SI card defines the angle of the cone with a range from  $\frac{1+\cos\theta}{2}$  to  $\frac{1-\cos\theta}{2}$  (X-5 Monte Carlo Team, 2008). The SP card modified the weight associated

with the particle tally. For the electron point source simulations the cone angle was set to 15 degrees illustrated in Figure 24. This allowed for full irradiation of the target point, observed in Figure 24 in red, and eliminated any electrons or secondary particles that would not interact with the target material. For the photon point source simulations the cone angle was set to 90 degrees. This angle was established due to the use of an F5 tally.

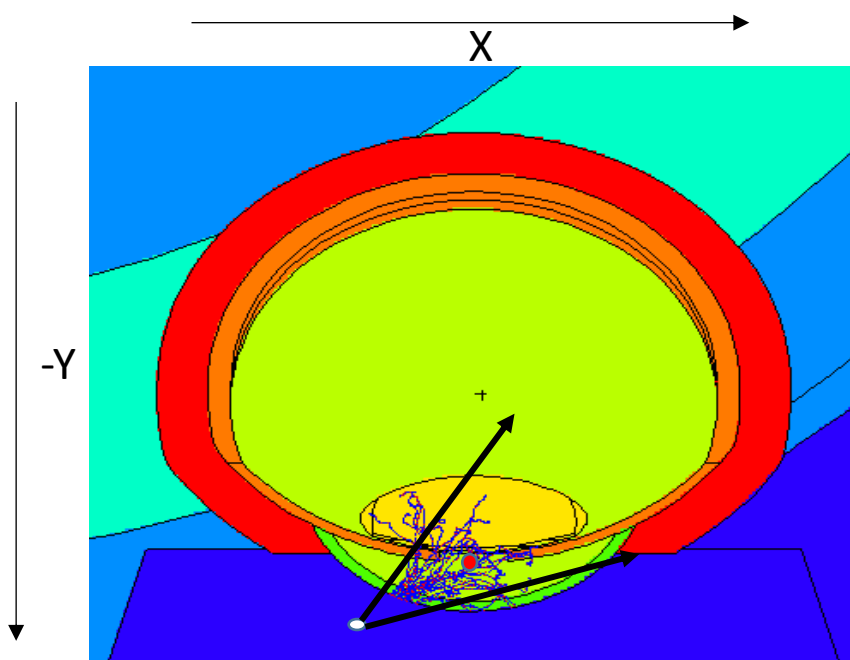


Figure 24: Illustration of 15 degree Cone for Electron Source

### 3.4 MCNP6 Tallies

#### 3.4.1 +F6 Tally for Electron Simulations

MCNP has several different tallies, which can be included into an input file and yield different information depending on the type of tally used. For the purposes of this study, a +F6 tally was used for electron point source simulations and a F5 tally was used for photon point source simulations. A +F6 tally scores a particle's energy that enters the tally medium and subtracts from the score once the particle exits the medium. Secondary

particles created in the medium will have their energies subtracted from the total tally score if they leave the tally medium. If a particle is totally absorbed in the medium the tally does not need to subtract any score (Boozer, 2018). The +F6 tally results in a measurement of energy deposition per source particle with the units of MeV/g. When multiplied by the constant  $1.60218^{-10} \frac{\text{J}\cdot\text{g}}{\text{MeV}\cdot\text{kg}}$ , the tally will result in a value of absorbed dose (units of Gy).

### 3.4.2 F5 Tally for Photon Simulations

An F5 tally is a point detector tally, which measures the photon fluence of a source in units of  $\frac{\text{particles}}{\text{cm}^2}$ . An F5 tally is a next event estimator and estimates the flux at a point as if the next event would lead the particle trajectory to the detector (X-5 Monte Carlo Team, 2008). When an F5 tally is utilized in a simulation to measure KERMA a dose energy/dose function (DE/DF) card must be included into the input file as a tally multiplier and is representative of the particle type and energy range defined in the source definition card. Using the correct DE/DF card will result in a measurement in the units of  $\frac{\text{J/kg}}{\text{photon}}$ . Table 2 displays the DE/DF values included in the input file. In addition to utilizing the correct DE/DF card for the F5 tally calculation purposes the distance between the photon point source and the target needed to be determined to evaluate if charged particle equilibrium had been achieved.

Dose Energy (MeV)	DF	Dose Energy (MeV)	DF	Dose Energy (MeV)	DF
0.05	1.20E-07	0.4	7.69E-07	3.0	4.00E-06
0.06	1.11E-07	0.5	9.09E-07	4.0	4.76E-06
0.08	1.20E-07	0.6	1.14E-06	5.0	5.56E-06
0.1	1.47E-07	0.8	1.47E-06	6.0	6.25E-06
0.15	2.38E-07	1.0	1.79E-06	8.0	7.69E-06
0.2	3.45E-07	1.5	2.44E-06	10.0	9.09E-06
0.3	5.56E-07	2.0	3.03E-06		

Table 2: Dose Energy/Dose conversion Values

### 3.4.2 Fractional CPE Evaluation

Fractional charged particle equilibrium ( $f_{CPE}$ ) is a value that can be used to determine dose if CPE has not been established and absorbed dose occurs in the buildup region. Since the distance between the photon point source and the target point in the eye may not be long enough for CPE to be established, a calculation must be performed to determine the distance a photon must travel in the eye corresponding to the absolute distance of the source. This assessment requires two variables to be assessed: the straight-line distance ( $x$ ) a photon travels after it penetrates the material until it reaches the target point (T) and the incident angle ( $\theta$ ) of the photon as it penetrates the material. Figure 25 depicts the relationship between the photon point source (S), the center of the cornea (O), the distance between the center of the cornea and the target point (t), and the location of the target point (T), and a reference point (C):

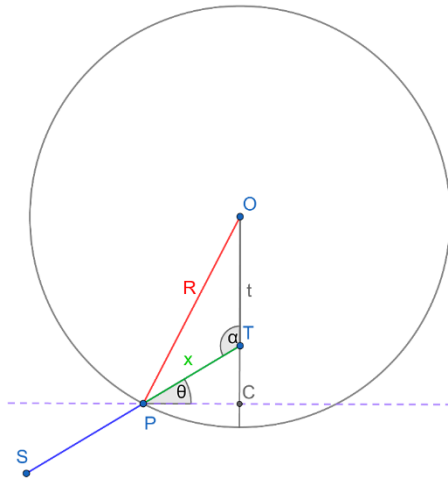


Figure 25: Fractional CPE Variable Considerations (Boozer, 2018)

To determine the penetration depth,  $x$ , a photon travels before reaching the target point consider the following. Let the source be at point  $(S_x, S_y)$  and target at point  $(t_x, t_y)$ . The incident angle between the source and T, is illustrated in equation 3.1:

$$\theta = \begin{cases} \tan^{-1} \left| \frac{t_y - s_y}{t_x - s_x} \right| & s_x \neq t_x \\ 90^\circ & s_x = t_x \end{cases} \quad (3.1)$$

Next, the law of cosines may be utilized and rearranged illustrated by equations 3.2 and 3.3:

$$R^2 = x^2 + t^2 - 2tx \cos \alpha \quad (3.2)$$

$$0 = x^2 + 2tx \sin \theta + t^2 - R^2 \quad (3.3)$$

Finally, the quadratic formula can be used to solve for  $x$  and only the positive value for  $x$  is needed illustrated by equation 3.4:

$$x = -t \sin \theta + \sqrt{(t \sin \theta)^2 - (t^2 - R^2)} \quad (3.4)$$

A relationship exists between the penetration depth and the incident angle from the eye model. The penetration depth is at 3 mm when the incident angle is  $90^\circ$ . As the incident angle deviates from  $90^\circ$  in either direction the amount of material the particles must penetrate to reach the lens increases, which results in conditions closer to CPE. Figure 26 shows the penetration depth as a function of the incident angle:

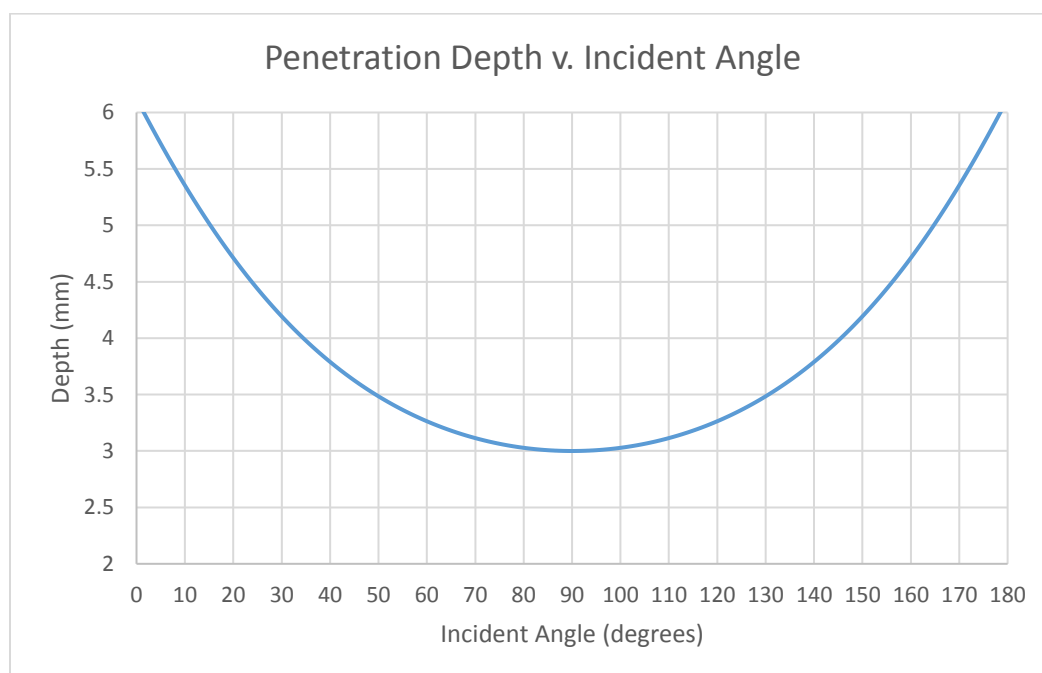


Figure 26: Penetration Depth vs. Incident Angle (Boozer, 2018)

These penetration depths can be compared to MCNP simulations. Boozer (2018) developed an empirical formulation for the estimation of  $f_{CPE}$ . If the distance a given energy photon must travel falls in the buildup region, the ratio of KERMA and absorbed dose will account for  $f_{CPE}$  and this value will be included in a deterministic model to evaluate absorbed dose to the target point in the eye from photons.

### 3.5 Deterministic Equation Development

#### 3.5.2 Table Curve 2D

To develop a deterministic model for photons which estimates the absorbed dose curve fitting software was utilized. TableCurve 2D is a statistical and graphics software package, which fits equations to linear and non-linear models generated in a two-dimensional plane (TableCurve2D, 2018). The user must upload a data sheet formatted per TableCurve 2D software requirements, so that the software may read the data and generate the respective model. There are several models generated by the TableCurve 2D software and include several output equations. The user may evaluate the equations and determine which model and equation fits best with the data uploaded into the TableCurve 2D software. Figure 27 is an example of a model generated from a data set uploaded into the TableCurve 2D software:

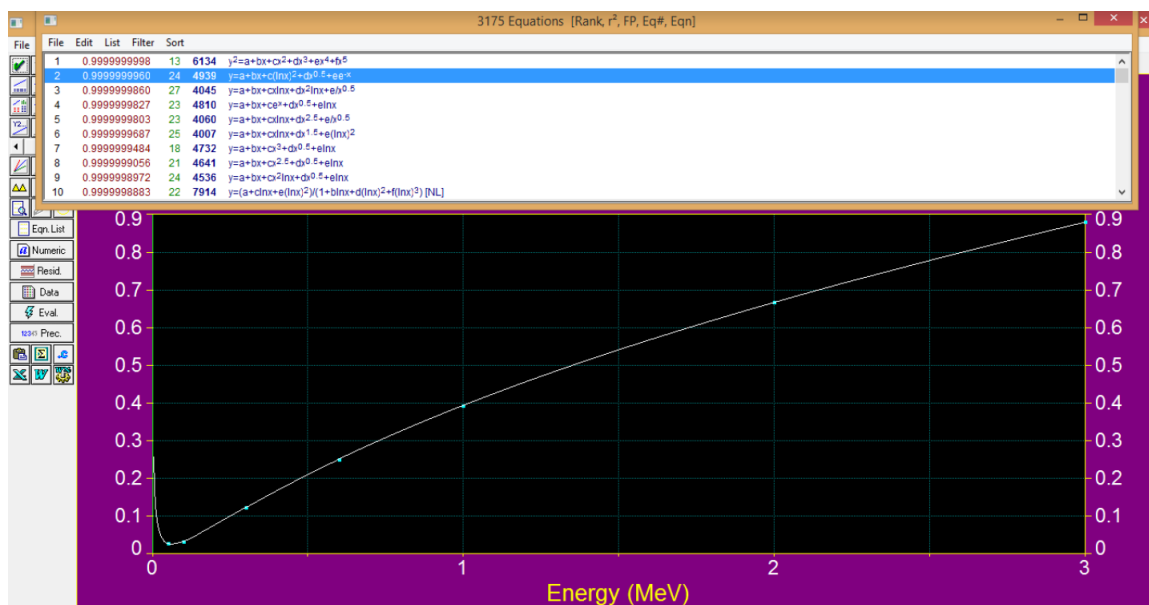


Figure 27: Illustration of TableCurve 2D Equation Output (TableCurve2D, 2018)

Once an equation is selected, it may be placed into a data sheet, in order to evaluate how well the equation generated from TableCurve 2D fits the data obtained from MCNP photon simulations. When there is good agreement between the TableCurve 2D equation and the obtained data, the equation becomes a coefficient in a new absorbed dose equation.

## Chapter 4 – Results and Discussion

### 4.1 Electrons

By Monte Carlo simulation, the target point in the eye was irradiated by electrons with energies of 0.8, 0.9, 1, 2, and 3 MeV. The source was moved in 0.1 cm increments, along the X-axis and in 0.05 cm increments along the Y-axis and the electron dose was assessed 121 times. The source was moved symmetrically on either side of the centerline position. Figure 28 is an illustration of each position the electron source was moved.

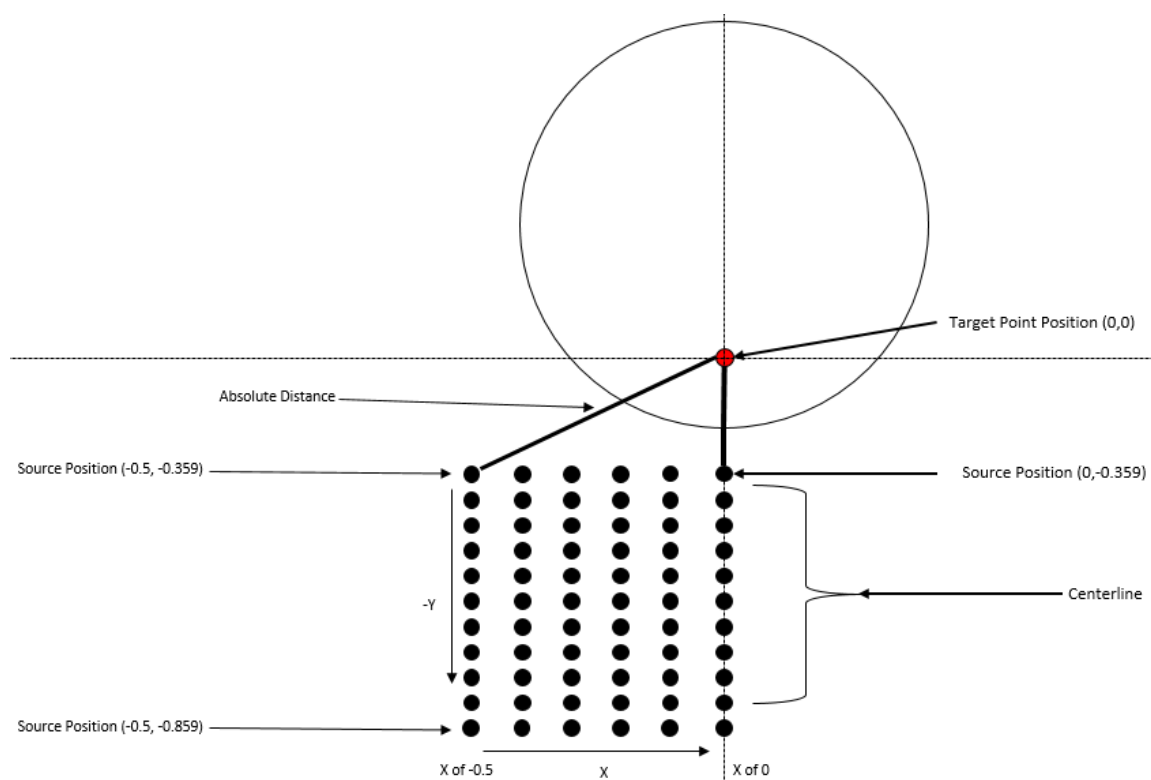


Figure 28: Position of Source Relative to Target Point

There was a uniform distribution of electron dose on either side of the centerline position of the source associated with each electron energy (Figure 29). Electron dose distributions for electrons between 0.8 and 2 MeV are located in Appendix A.

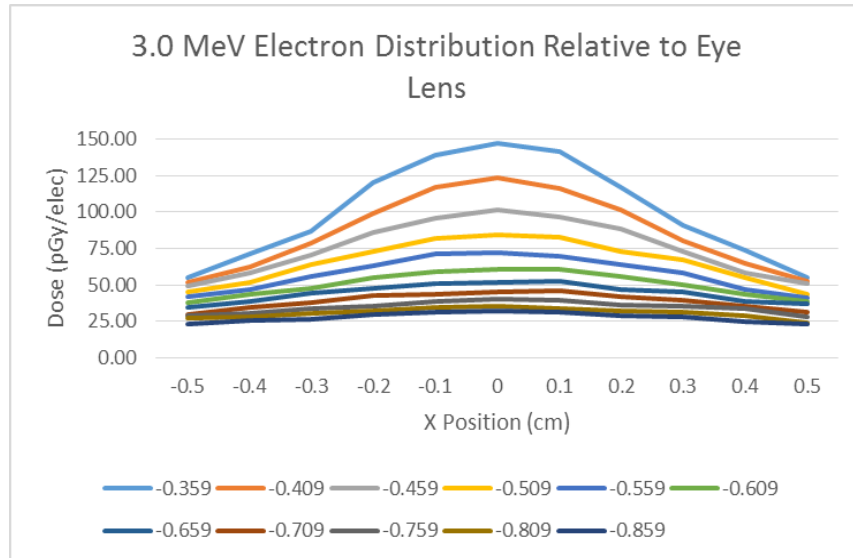


Figure 29: Y Positions of 3 MeV Electron Source

Since the dose is symmetric relative to the center of the eye the values for electron doses were averaged based on their corresponding X and Y positions. The maximum relative errors associated with each electron energy simulation are listed in Table 3:

Greatest Relative Error	
0.8 MeV Electrons	9%
0.9 MeV Electrons	8.22%
1.0 MeV Electrons	2.91%
2.0 MeV Electrons	2.85%
3.0 MeV Electrons	4.15%

Table 3: Greatest Relative Error for Electrons

The lower energy electron simulations had a greater relative error observed, because the maximum range of the lower energy electrons prevented them from reaching the target point in most cases.

For example, the eye was irradiated by a 0.8 MeV electron point source. The maximum range for a 0.8 MeV electron is approximately 0.309 cm, only slightly greater than the assumed thickness of the cornea and anterior chamber. Due to this short range, the energy deposited was likely from the fraction of kinetic energy of the electron that was converted to bremsstrahlung, about 0.36% of the original energy. Figure 30 illustrates the maximum range of a 0.8 MeV electron penetrating the eye at an absolute distance of 0.359 cm. Notice that no electrons actually reach the target point marked as a red point.

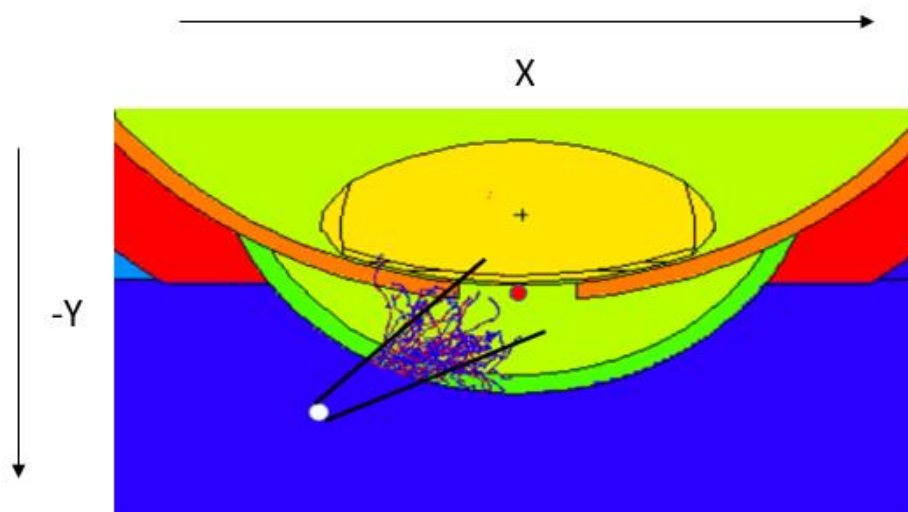


Figure 30: Maximum Range of a 0.8 MeV Electron Particle in the Eye

The data associated with each electron energy simulation was collected and evaluated with the X-coordinate position held constant for the given simulations. As the source was moved in the negative Y-direction, away from the eye, the absolute distance

increased between the source and target point. When there is an increase in absolute distance between the source and target point on either side of the centerline position the distance the electron needed to penetrate the eye to reach the target position was reduced. This is due to the relationship between the incident angle and source position effecting the penetration depth. As the Y-position of the source moves away from the target the incident angle where  $\theta \neq 0$ , increases and is associated with a reduced penetration distance the electron must travel to reach the target point. In addition to the amount of air and eye tissue the electron must traverse to deposit dose there is a change in stopping power and energy degradation occurs, which is noticeable as the electron source departs from the centerline position.

As an electron penetrates the eye, deceleration occurs and the stopping power increases. When an electron reaches half of its maximum range, the stopping power of the electron is at its maximum value, which is a consequence of the range straggling associated with an electron. As you can see in Figure 31 each position of the source results in an eye lens dose peak, followed by a steady decrease with the exception of the source positioned at the centerline position directly in front of the eye. When the source is positioned at the centerline position there is only a steady decrease in average eye lens dose, since there is only an increase in distance the electron must travel in dry air and the penetration depth is constant. Similar trends were observed for electrons between 0.8 MeV to 3.0 MeV and may be found in Appendix B.

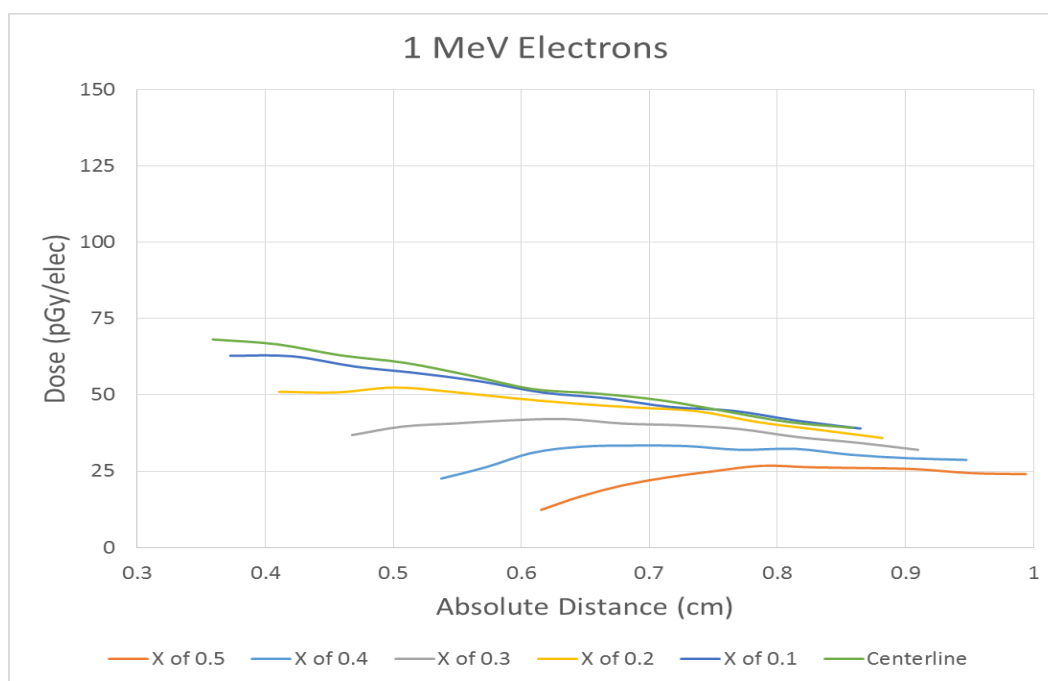


Figure 31: Dose from 1 MeV Electrons as Absolute Y-Distance Increases

Due to the irregularities associated with each electron equation, but noticing similar trends associated with each simulation of electrons with respect to energy and absolute distance of the source, dose tables were generated. The dose tables for each electron energy simulation are located in Appendix C. The electron dose tables may be utilized to assess absorbed dose to the eye lens from an electron between the energies of 0.8 to 3.0 MeV. Linearity may be assumed, so that linear interpolation may be performed to assess absorbed dose to the eye lens. An MCNP simulation was performed for a 1.5 MeV electron at an absolute distance of 0.6648 cm to evaluate how well the interpolated between data for 1 MeV and 2 MeV electrons agreed with the MCNP simulation. This relationship may be observed in Table 4:

MCNP Values vs. Predicted Values					
Electron Energy (MeV)	Absolute Distance (cm)	MCNP Lens Dose (pGy/elec)	Interpolated Predicted Value (pGy/elec)	Absolute Difference (pGy/elec)	Relative Difference (%)
1.5	0.6648	48.55	50.16	1.61	3.26

Table 4: MCNP Values Obtained for Electron Energies and Absolute Distances

#### 4.2 Photons

The target point in the eye was irradiated by photons of energies 0.05, 0.1, 0.3, 0.6, 1, 2, and 3 MeV. The photon source was moved in an identical manner as the electron sources mentioned earlier. Each simulation was performed for the respective energy and then plotted as KERMA compared to absolute distance (Figure 32). The greatest relative error for each photon's energy is observed in Table 5:

Photon Energy (MeV)	Greatest Relative Error (%)
3	0.93
2	0.26
1	0.21
0.6	0.19
0.3	0.21
0.1	0.33
0.05	0.26

Table 5: Greatest Relative Error for each Photon Simulation

The curves illustrated in Figure 32 are arranged in descending order starting from 3 MeV photons and ending with 0.05 MeV photons:

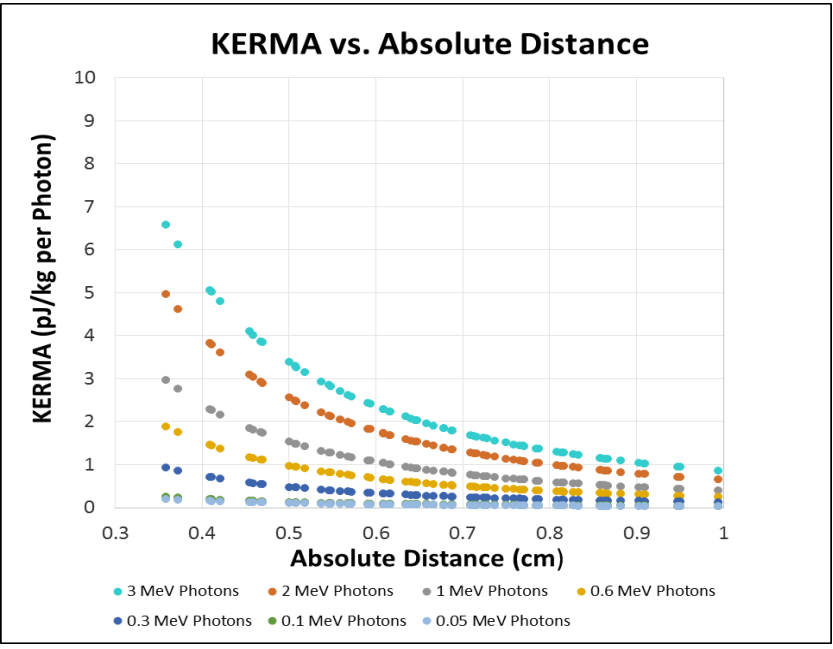


Figure 32: KERMA vs. Absolute Distance

In order to verify the power rule was appropriately identified a check was performed converting the values from Figure 32 to a logarithmic scale. The results were linear functions with equivalent slopes for each respective photon energy (Figure 33). Each line has a slope of -2 corresponding to the power rule  $\left(\frac{1}{r^2}\right)$ , where  $r$  is the distance from the source to target:

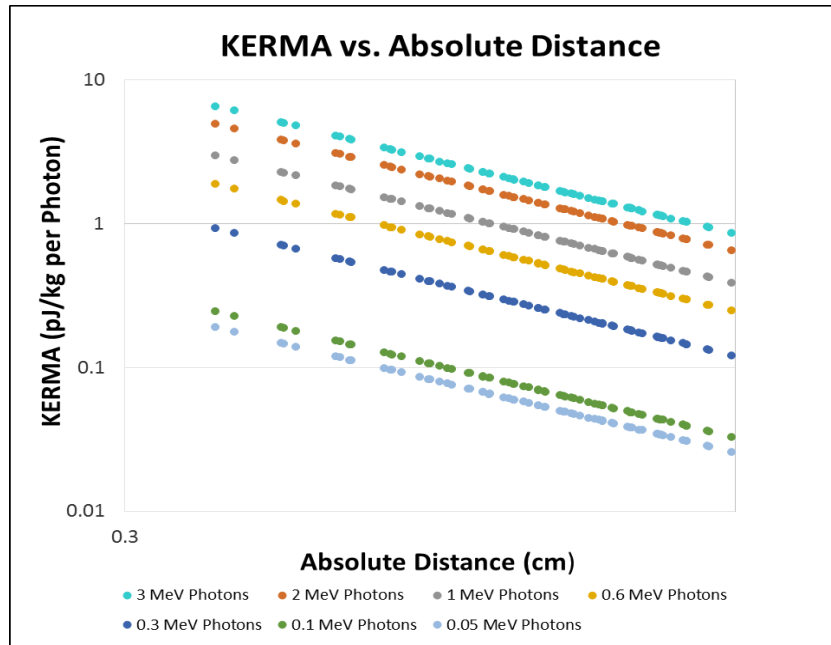


Figure 33: Logarithmic Scale Check of Photon Power Rule

Once the relationship among photons was evaluated it was confirmed that lens dose from photons is energy dependent. To develop a deterministic equation for the absorbed dose to the eye lens from photons TableCurve2D was utilized. A function was found to be in the best agreement with an  $R^2$  of 0.9999995848 from the data obtained from photon simulations in MCNP (Equation 4.1):

$$A(E) = a + b\sqrt{E} + cE + dE^{1.5} + fE^2 + gE^{2.5} \quad (4.1)$$

Where,  $A(E)$ , is the new photon coefficient as a function of photon energy,  $E$ , (in MeV) represents photon energy with respect to the absolute distance between the photon and target point. The coefficients  $a$ ,  $b$ ,  $c$ ,  $d$ ,  $f$ , and  $g$  are coefficients with values of:

Coefficients	Value
a	0.16956
b	-1.3281
c	3.8959
d	-3.898
f	1.899
g	-0.3558

Table 6: Coefficient Data Table

Therefore, to determine KERMA to the target point corresponding to the absolute distance a photon source is away from the target point use equation 4.2:

$$KERMA = \frac{a+b\sqrt{E}+cE+dE^{1.5}+fE^2+gE^{2.5}}{r^2} \quad (4.2)$$

Finally, the equation for photon eye lens dosimetry was used to examine its fit to obtained data from MCNP and then checked to see how it would fit to a photon with energy of 3 MeV (Figure 34):

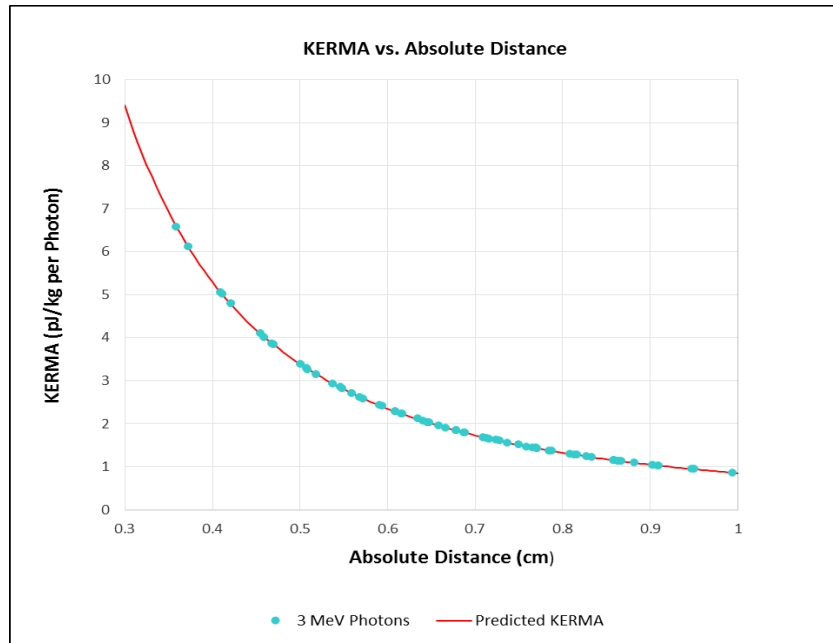


Figure 34: KERMA vs. Absolute Distance of 3 MeV Photons

KERMA can be converted to absorbed dose if CPE is established where absorbed dose and KERMA are equal or a value for fractional CPE is introduced to determine the absorbed dose in the buildup region. Most of the energy absorption from photons for energies above 0.5 MeV occurs in the buildup region and the fractional CPE must be included, so that absorbed dose may be determined from KERMA estimation (Boozer, 2018).

Once CPE or fractional CPE has been assessed for each photon energy and source position, it can be included into the new absorbed dose equation. The inclusion of fractional CPE will result in the dose in the buildup region ( $D_{BU}$ ):

$$D_{BU} = KERMA \cdot f_{cpe} = \frac{a+b\sqrt{E}+cE+dE^{1.5}+fE^2+gE^{2.5}}{r^2} \cdot f_{cpe} \quad (4.3)$$

## Chapter 5 - Conclusion

Since the ICRP recommended a revision to the lens dose limits in ICRP Publication 118 (Stewart, 2012) the radiation protection community has conducted many new studies related to eye dosimetry. The recommended reduction of eye lens dose limits may result in the reduction of the whole body dose limit, which effects all occupational workers in the nuclear science and engineering industries. The need for further investigative research into eye dosimetry is due to the formation of radio induced cataracts and eye degradation from ionizing radiation. Radiation workers are in frequent proximity to ionizing radiation sources and their eyes are susceptible to radiation damage.

The aim of this research was to investigate how distance, incident angle, particle type, and energy effect the energy deposited to a target point in the eye from electron and photon point sources. A lens depth of  $300 \text{ mg/cm}^2$  as defined by the Nuclear Regulatory Commission was incorporated into this study. Our data have been utilized to evaluate absorbed dose from electron and photon point sources and derive eye lens dose tables for electrons and a deterministic model for photon sources that can be used for eye dosimetry. The sources were placed in positions along a Cartesian coordinate system close to the eye relative to anticipated occupational exposure scenarios with approximate angles between 35 to 90 degrees.

An observation was made for electrons that the absorbed dose to the target point in the eye for a given electron energy depicted a maximum dose peak for each respective

X-Coordinate position other than the centerline position. This is due to the maximum stopping power of an electron occurring at half of the maximum range of the electron in the eye. When the source was moved further distances from the eye there was less energy degradation observed, because more energy degradation occurs in the eye, than air. Since the absolute distance associated with the electron source position greatly affected the absorbed dose to the target point a deterministic equation to assess electron eye dosimetry could not be derived at this time. However, the data obtained from this study was sufficient in developing electron eye dosimetry tables, which can be interpolated among electron data points. The interpolated electron dose was within good agreement of MCNP simulated data.

Photon absorbed dose was found to be impacted from absolute distance between the source to reach the target point. Although the distance from the source to the target point effected the absorbed dose from photons each photon absorbed dose was found to trend in an inverse distance squared function. Since, photon absorbed dose was found to be inversely proportional to the distance squared from the source position and a constant value, a deterministic equation was derived from the MCNP simulation data and the use of an equation fitting software. The equation was found to be in good agreement with all of the data points associated with each photon simulation. The empirically developed  $f_{CPE}$  formulation was incorporated into the absorbed dose equation to account for photon doses in the buildup and transient regions.

From this study there are several recommendations for future research into developing deterministic equations for electron dosimetry and perfecting deterministic

equations for photon dosimetry. First, the research could uncouple the variables associated with absorbed dose to the lens for electrons and assess how each variable contributes to absorbed dose to assist in developing a deterministic equation. Next, the deterministic equation for photons could be assessed with the inclusion of shielding materials to see if the equation is still valid. A simplification of this study could be performed if the researcher were to use a beam source as opposed to a point source. Finally, further research could take into account how eye accommodation, which is the process of the lens focusing on a point, could impact dose to the lens of the eye.

## References

- Attix, F., & Wiley InterScience. (1986). Introduction to radiological physics and radiation dosimetry. New York: Wiley.
- Behrens, R., & Dietze, G. (2011). Dose conversion coefficients for photon exposure of the human eye lens. *Physics in Medicine and Biology*, 56(2), 415-437.
- Boozer, D. (2018). Absorbed Dose and KERMA. Retrieved on May 15, 2018. Retrieved from file:///C:/Users/Ian/Downloads/Absorbed%20Dose%20and%20KERMA%20.pdf.
- Bolch, W., Dietze, G., Petoussi-Henss, N., & Zankl, M. (2015). Dosimetric models of the eye and lens of the eye and their use in assessing dose coefficients for ocular exposures. *Annals of the ICRP*, 44(1\_suppl), 91-111.
- Charles, M.W. and Brown, N. (1975). Dimensions of the human eye relevant to radiation protection (dosimetry). *Physics in Medicine and Biology*, 20(2), 202-218.
- Carlson, T. (2013). Photoelectron and Auger spectroscopy. Springer Science & Business Media.
- Czarwinski, R. (2013). Implications of the implementation of the reduced dose limits for the lens of the eye: an IRPA activity. *Journal of Radiological Protection*, 33(4), E15.
- De-Shalit, A., Talmi, Igal, & Massey, H. S. W. (2014). Nuclear Shell Theory. Saint Louis: Elsevier Science.
- Eckerman, K.F., Cristy, M., and Ryman, J. C. (1996). The ORNL mathematical phantom series, available at: <http://ornl.gov/vlab/mird2.pdf>.
- Geber, Gunnarsson, & Mattsson. (2011). Eye lens dosimetry for interventional procedures – Relation between the absorbed dose to the lens and dose at measurement positions. *Radiation Measurements*, 46(11), 1248-1251.
- Gualdrini, Mariotti, Wach, Bilski, Denoziere, Daures, . . . Vanhavere. (2011a). A new cylindrical phantom for eye lens dosimetry development. *Radiation Measurements*, 46(11), 1231-1234.
- Gualdrini, Mariotti, Wach, Bilski, Denoziere, Daures, . . . Fantuzzi. (2011b). Eye lens dosimetry: Task 2 within the ORAMED project. *Radiation Protection Dosimetry*, 144(1-4), 473-477.
- Hall, E., & Giaccia, Amato J. (2012). Radiobiology for the radiologist (7th ed.). Philadelphia: Wolters Kluwer Health/Lippincott Williams & Wilkins.

- Hamby, D. M., Mangini, C. D., Caffrey, J. A., Tang, M. (2014). VARSKIN 5: A Computer Code for Skin Contamination Dosimetry. *NUREG/CR-6918 Revision 2*. Washington, DC: U.S. Nuclear Regulatory Commission.
- Patton, W. P., Gillespie, H. C., Frew, L., Burns, M. T., Lewis, S. E., & Chakravarthy, U. (2002). The effects of high ambient glucose on the radiosensitivity of retinalmicrovascular endothelial cells and pericytes. *Current Eye Research*, 24(1), 51.
- Krane, K. (2012). *Modern physics* (Third ed.). Hoboken, NJ: Wiley.
- Krstić, & Nikezić. (2007). Input files with ORNL—mathematical phantoms of the human body for MCNP-4B. *Computer Physics Communications*, 176(1), 33-37.
- Martin, J., & Wiley InterScience. (2006). *Physics for radiation protection : A handbook* (2nd ed., rev. and enl. ed.). Weinheim: Wiley-VCH.
- Nogueira, Zankl, Schlattl, & Vaz. (2011). Dose conversion coefficients for monoenergetic electrons incident on a realistic human eye model with different lens cell populations. *Physics in Medicine and Biology*, 56(21), 6919-6934.
- Nuclear Regulatory Commission. (2018). Lens Dose Equivalent. Retrieved on April 14, 2018. Retrieved from <https://www.nrc.gov/reading-rm/basic-ref/glossary/lens-dose-equivalent.html>.
- Pfutzner, M., Karny, M., Grigorenko, L. V., & Riisager, K. (2012). Radioactive decays at limits of nuclear stability.(Report). *Reviews of Modern Physics*, 84(2), 567-619.
- Seals, K. (2016). Radiation-Induced Cataractogenesis: A Critical Literature Review for the Interventional Radiologist. *Cardiovascular and Interventional Radiology*, 39(2), *Cardiovascular and Interventional Radiology*, 2016, Vol.39(2).
- Shultis, J. K., & Faw, R. E. (2007). *Fundamentals of nuclear science and engineering*. Boca Raton: CRC Press.
- Stewart, F.A, Akleyev, A.V, Hauer-Jensen, M, Hendry, J.H., Kleiman, N.J., MacVittie, T.J., Aleman, B.M., Edgar, A.B., Mabuchi, K., Muirhead, C.R., Shore, R.E., Wallace, W.H. (2012). ICRP PUBLICATION 118: ICRP Statement on Tissue Reactions and Early and Late Effects of Radiation in Normal Tissues and Organs — Threshold Doses for Tissue Reactions in a Radiation Protection Context. *Annals of the ICRP*, 41(1-2), 1-322.
- TableCurve 2D: Automated Curve fitting software [Computer Software]. (2018). Retrieved from <https://systatsoftware.com/products/tablecurve-2d/>
- Willoughby, C. E., Ponzin, D., Ferrari, S., Lobo, A., Landau, K., & Omid, Y. (2010). Anatomy and physiology of the human eye: effects of mucopolysaccharidoses disease on structure and function – a review. *Clinical & Experimental Ophthalmology*, 382-11. doi:10.1111/j.1442-9071.2010.02363.x

Worgul, B.V. (1991). The Edward S Harkness Eye Institute Resident's Basic Science Study Guide (New York: Columbia University Press)

X-5 Monte Carlo Team. (2008). MCNP – A General Monte Carlo N-Particle Transport Code, Version 5. LA-UR-03-1987, Los Alamos National Laboratory.

APPENDICES

APPENDIX A: Electron Distribution Curves

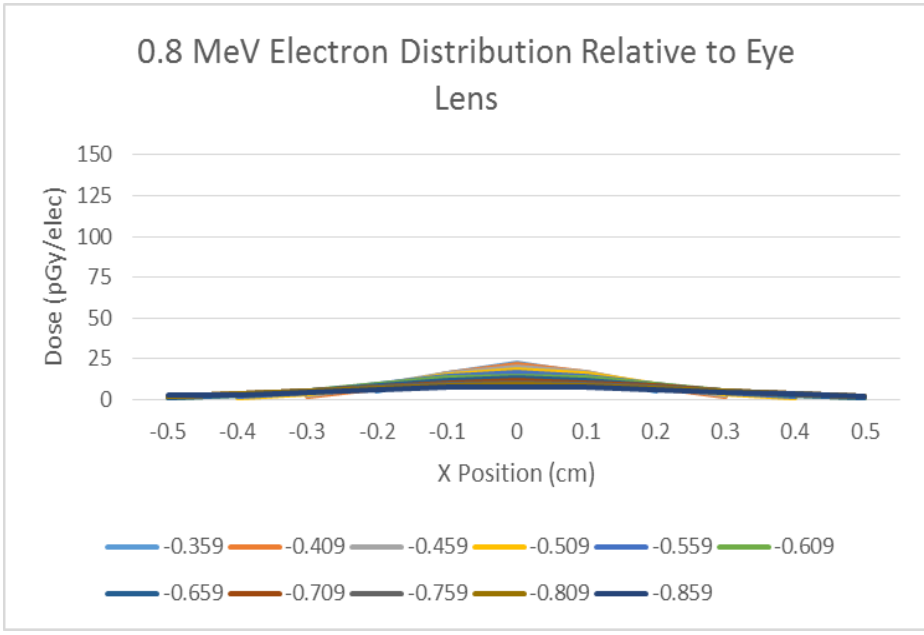


Figure A. 1: 0.8 MeV Electron Distribution Relative to Eye Lens

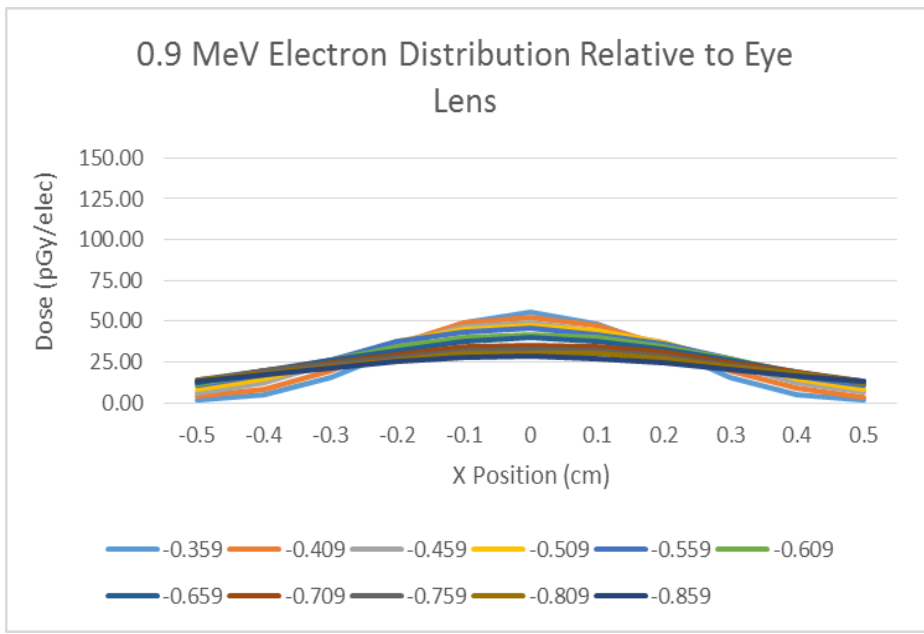


Figure A. 2: 0.9 MeV Electron Distribution Relative to Eye Lens

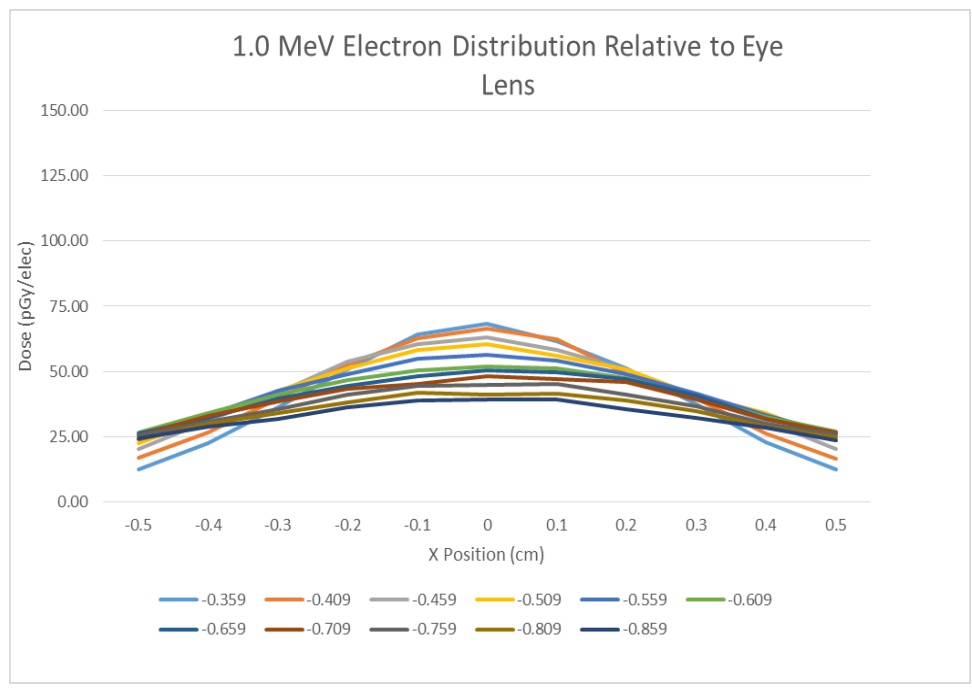


Figure A. 3: 1 MeV Electron Distribution Relative to Eye Lens

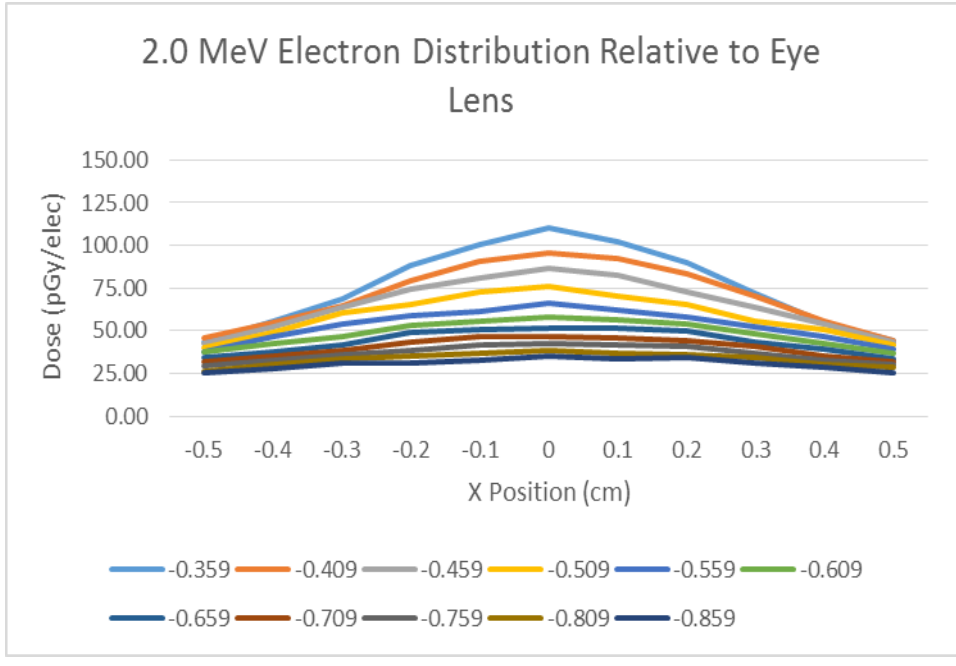


Figure A. 4: 0.9 MeV Electron Distribution Relative to Eye Lens

## APPENDIX B: Electron Energies vs. Absolute Distance with Respect to X-Axis

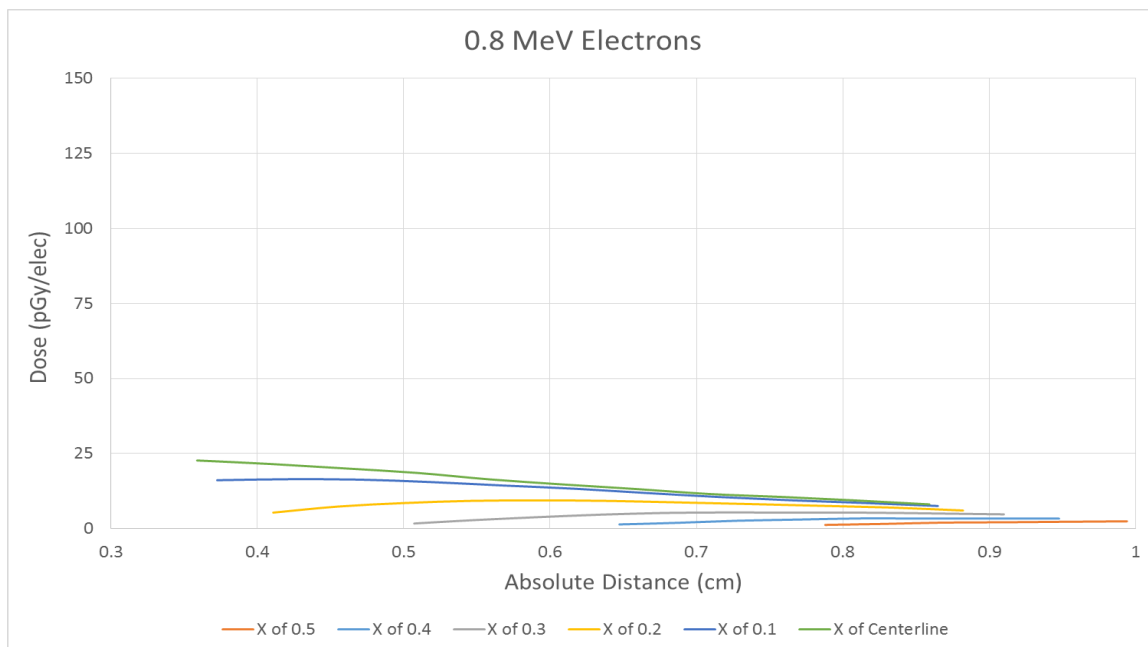


Figure A. 5: Dose from 0.8 MeV Electrons as Absolute Y-Distance Increases

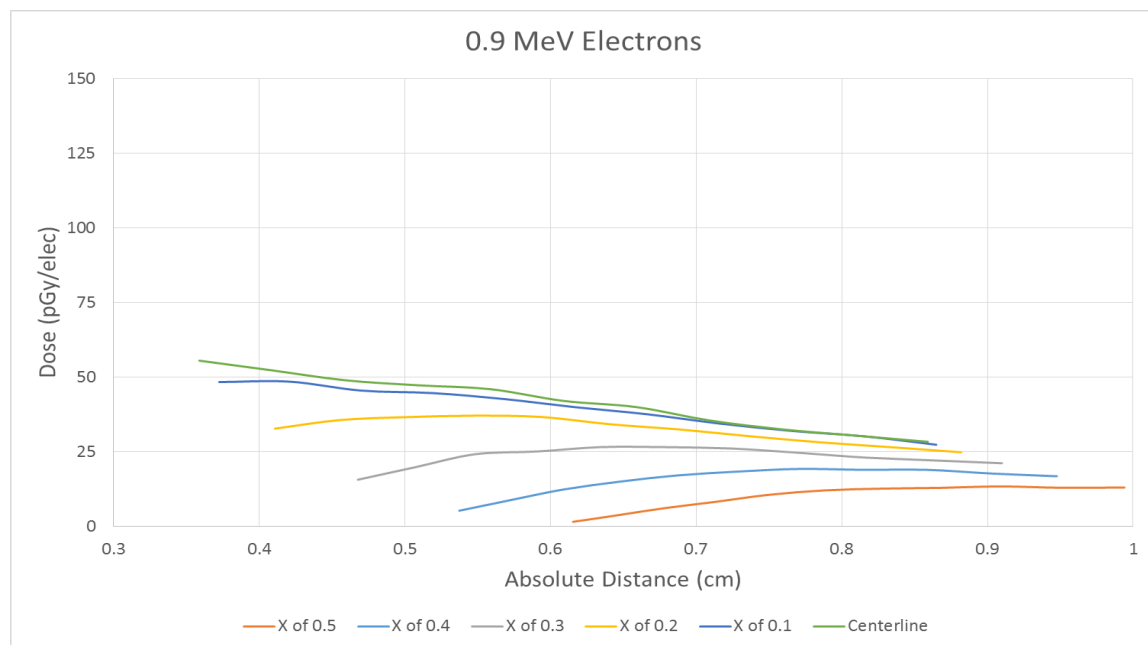


Figure A. 6: Dose from 0.9 MeV Electrons as Absolute Y-Distance Increases

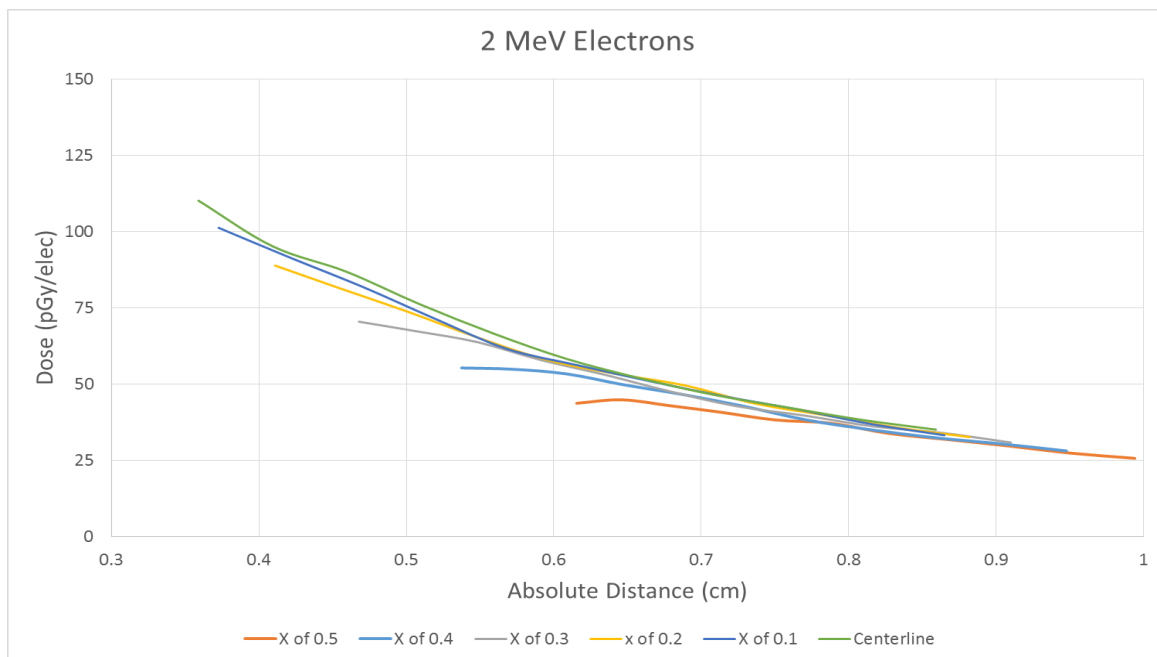


Figure A. 7: Dose from 2 MeV Electrons as Absolute Y-Distance Increases

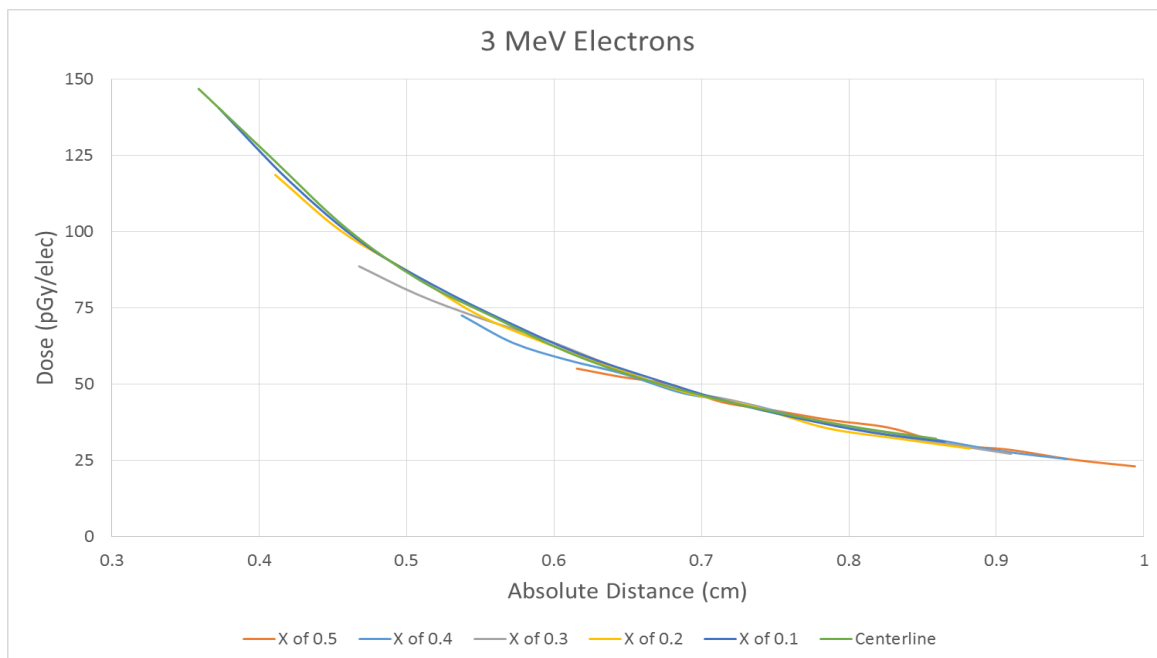


Figure A. 8: Dose from 3 MeV Electrons as Absolute Y-Distance Increases

## APPENDIX C: Electron Eye Lens Dose Tables

Absolute Distance (cm)	Thickness of Eye (cm)	Average Target Point Dose (pGy per electron)
0.359	0.3	22.7099
0.372667412	0.306867324	16.1414
0.409	0.3	21.5352
0.410951335	0.324767735	5.34696
0.421047503	0.305336343	16.4675
0.455281232	0.319667044	7.38018
0.459	0.3	20.0954
0.469766964	0.304262441	16.32945
0.500680537	0.315956736	8.53977
0.507228745	0.339274498	1.727825
0.509	0.3	18.5846
0.51873018	0.303481198	15.509
0.546882986	0.313184492	9.26264
0.54834387	0.332524334	2.85797
0.559	0.3	16.4023
0.567874106	0.302895656	14.382
0.590830771	0.32730311	3.81724
0.593701103	0.311064417	9.434395
0.609	0.3	14.7234
0.617155572	0.302445763	13.2847
0.634413903	0.3232001	4.666275
0.641	0.309409999	9.23834
0.647364658	0.343799746	1.422405
0.659	0.3	13.2058
0.666544072	0.302092778	11.8662
0.678882169	0.319928212	5.25025
0.687372534	0.337740454	1.9536
0.688680623	0.308096002	8.727485
0.709	0.3	11.5405
0.716017458	0.301810822	10.5321
0.72407251	0.317283805	5.39701
0.728615811	0.332791568	2.646595
0.736668854	0.30703612	8.20137
0.759	0.3	10.5425
0.765559273	0.30158209	9.42995
0.769857779	0.315120208	5.3495
0.770896232	0.328711456	3.037555
0.784908275	0.306169475	7.62074
0.787960024	0.346867306	1.256735
0.809	0.3	9.38746
0.81405221	0.325317192	3.426845
0.81515704	0.301394013	8.552435
0.816137856	0.313330165	5.325325
0.82721279	0.341447359	1.579955
0.833355266	0.305452214	7.01303
0.85795163	0.322469323	3.36209
0.859	0.3	8.09958
0.862833124	0.311834096	5.059375
0.864801133	0.301237516	7.555865
0.867571899	0.336859987	2.0079
0.881975623	0.304852153	6.049225
0.902486011	0.32006068	3.35207
0.908889982	0.332953399	2.11487
0.909879662	0.31057213	4.77162
0.947565829	0.318008204	3.34767
0.95104206	0.329606546	2.289605
0.993922029	0.326722556	2.45424

Table A.1: 0.8 MeV Electron Eye Lens Dose Table

Absolute Distance (cm)	Thickness of Eye (cm)	Average Target Point Dose (pGy per electron)
0.359	0.3	55.4842
0.372667412	0.306867324	48.3157
0.409	0.3	52.2301
0.410951335	0.324767735	32.7355
0.421047503	0.305336343	48.4531
0.455281232	0.319667044	35.57625
0.459	0.3	48.9282
0.467847197	0.348148681	15.60975
0.469766964	0.304262441	45.4735
0.500680537	0.315956736	36.55655
0.507228745	0.339274498	19.79715
0.509	0.3	47.2398
0.51873018	0.303481198	44.63215
0.537476511	0.372411443	5.224875
0.546882986	0.313184492	37.0542
0.54834387	0.332524334	24.1466
0.559	0.3	45.9198
0.567874106	0.302895656	42.6469
0.572084784	0.360638855	8.71943
0.590830771	0.32730311	25.0548
0.593701103	0.311064417	36.6148
0.608835774	0.351290274	12.32085
0.609	0.3	42.0019
0.615533102	0.395086552	1.50211
0.617155572	0.302445763	39.89665
0.634413903	0.3232001	26.5329
0.641	0.309409999	34.1766
0.64597291	0.381490544	3.69704
0.647364658	0.343799746	14.94115
0.659	0.3	39.9311
0.666544072	0.302092778	37.5237
0.678734853	0.370285846	6.10875
0.678882169	0.319928212	26.5203
0.687372534	0.337740454	17.05195
0.688680623	0.308096002	32.4348
0.709	0.3	35.4724
0.713499124	0.361016724	8.20987
0.716017458	0.301810822	34.4198
0.72407251	0.317283805	26.05755
0.728615811	0.332791568	18.33715
0.736668854	0.30703612	30.17285
0.749987333	0.353310555	10.5601
0.759	0.3	32.4677
0.765559273	0.30158209	31.94895
0.769857779	0.315120208	24.63955
0.770896232	0.328711456	19.2163
0.784908275	0.306169475	28.14505
0.787960024	0.346867306	12.02885
0.809	0.3	30.4075
0.81405221	0.325317192	18.91825
0.81515704	0.301394013	30.15405
0.816137856	0.313330165	23.02765
0.82721279	0.341447359	12.61025
0.833355266	0.305452214	26.5223
0.85795163	0.322469323	18.90935
0.859	0.3	28.3229
0.862833124	0.311834096	22.0758
0.864801133	0.301237516	27.3271
0.867571899	0.336859987	12.8766
0.881975623	0.304852153	24.81375
0.902486011	0.32006068	17.6882
0.908889982	0.332953399	13.34865
0.909879662	0.31057213	21.1172
0.947565829	0.318008204	16.76
0.95104206	0.329606546	12.90815
0.993922029	0.326722556	13.0009

Table A. 2: 0.9 MeV Electron Eye Lens Dose Table

Absolute Distance (cm)	Thickness of Eye (cm)	Average Target Point Dose (pGy per electron)
0.359	0.3	55.4842
0.372667412	0.306867324	48.3157
0.409	0.3	52.2301
0.410951335	0.324767735	32.7355
0.421047503	0.305336343	48.4531
0.455281232	0.319667044	35.57625
0.459	0.3	48.9282
0.467847197	0.348148681	15.60975
0.469766964	0.304262441	45.4735
0.500680537	0.315956736	36.55655
0.507228745	0.339274498	19.79715
0.509	0.3	47.2398
0.51873018	0.303481198	44.63215
0.537476511	0.372411443	5.224875
0.546882986	0.313184492	37.0542
0.54834387	0.332524334	24.1466
0.559	0.3	45.9198
0.567874106	0.302895656	42.6469
0.572084784	0.360638855	8.71943
0.590830771	0.32730311	25.0548
0.593701103	0.311064417	36.6148
0.608835774	0.351290274	12.32085
0.609	0.3	42.0019
0.615533102	0.395086552	1.50211
0.617155572	0.302445763	39.89665
0.634413903	0.3232001	26.5329
0.641	0.309409999	34.1766
0.64597291	0.381490544	3.69704
0.647364658	0.343799746	14.94115
0.659	0.3	39.9311
0.666544072	0.302092778	37.5237
0.678734853	0.370285846	6.10875
0.678882169	0.319928212	26.5203
0.687372534	0.337740454	17.05195
0.688680623	0.308096002	32.4348
0.709	0.3	35.4724
0.713499124	0.361016724	8.20987
0.716017458	0.301810822	34.4198
0.72407251	0.317283805	26.05755
0.728615811	0.332791568	18.33715
0.736668854	0.30703612	30.17285
0.749987333	0.353310555	10.5601
0.759	0.3	32.4677
0.765559273	0.30158209	31.94895
0.769857779	0.315120208	24.63955
0.770896232	0.328711456	19.2163
0.784908275	0.306169475	28.14505
0.787960024	0.346867306	12.02885
0.809	0.3	30.4075
0.81405221	0.325317192	18.91825
0.81515704	0.301394013	30.15405
0.816137856	0.313330165	23.02765
0.82721279	0.341447359	12.61025
0.833355266	0.305452214	26.5223
0.85795163	0.322469323	18.90935
0.859	0.3	28.3229
0.862833124	0.311834096	22.0758
0.864801133	0.301237516	27.3271
0.867571899	0.336859987	12.8766
0.881975623	0.304852153	24.81375
0.902486011	0.32006068	17.6882
0.908889982	0.332953399	13.34865
0.909879662	0.31057213	21.1172
0.947565829	0.318008204	16.76
0.95104206	0.329606546	12.90815
0.993922029	0.326722556	13.0009

Table A. 3: 1 MeV Electron Eye Lens Dose Table

Absolute Distance (cm)	Thickness of Eye (cm)	Average Target Point Dose (pGy per electron)
0.359	0.3	110.138
0.372667412	0.306867324	101.233
0.409	0.3	95.2398
0.410951335	0.324767735	88.854
0.421047503	0.305336343	91.47595
0.455281232	0.319667044	81.32965
0.459	0.3	86.9029
0.467847197	0.348148681	70.44925
0.469766964	0.304262441	81.9869
0.500680537	0.315956736	73.77855
0.507228745	0.339274498	67.2936
0.509	0.3	76.1938
0.51873018	0.303481198	71.5592
0.537476511	0.372411443	55.2919
0.546882986	0.313184492	65.516
0.54834387	0.332524334	63.7508
0.559	0.3	66.5824
0.567874106	0.302895656	61.59565
0.572084784	0.360638855	54.86715
0.590830771	0.32730311	57.93685
0.593701103	0.311064417	58.1545
0.608835774	0.351290274	53.3307
0.609	0.3	58.211
0.615533102	0.395086552	43.7248
0.617155572	0.302445763	56.06885
0.634413903	0.3232001	53.07775
0.641	0.309409999	53.44485
0.64597291	0.381490544	44.8578
0.647364658	0.343799746	49.77845
0.659	0.3	51.8483
0.666544072	0.302092778	50.8109
0.678734853	0.370285846	42.9177
0.678882169	0.319928212	47.58695
0.687372534	0.337740454	46.5899
0.688680623	0.308096002	49.59345
0.709	0.3	46.4443
0.713499124	0.361016724	40.7671
0.716017458	0.301810822	45.9209
0.72407251	0.317283805	42.7352
0.728615811	0.332791568	42.76005
0.736668854	0.30703612	43.5963
0.749987333	0.353310555	38.2577
0.759	0.3	42.2874
0.765559273	0.30158209	41.68095
0.769857779	0.315120208	39.69605
0.770896232	0.328711456	38.2927
0.784908275	0.306169475	39.7229
0.787960024	0.346867306	37.16475
0.809	0.3	38.2671
0.81405221	0.325317192	35.09655
0.81515704	0.301394013	36.8995
0.816137856	0.313330165	36.1698
0.82721279	0.341447359	33.82505
0.833355266	0.305452214	35.71105
0.85795163	0.322469323	32.45205
0.859	0.3	35.0955
0.862833124	0.311834096	34.03885
0.864801133	0.301237516	33.24575
0.867571899	0.336859987	31.79665
0.881975623	0.304852153	32.63195
0.902486011	0.32006068	30.46185
0.908889982	0.332953399	29.69375
0.909879662	0.31057213	30.85045
0.947565829	0.318008204	28.09495
0.95104206	0.329606546	27.3453
0.993922029	0.326722556	25.67955

Table A. 4: 2 MeV Electron Eye Lens Dose Table

Absolute Distance (cm)	Thickness of Eye (cm)	Average Target Point Dose (pGy per electron)
0.359	0.3	146.869
0.372667412	0.306867324	140.572
0.409	0.3	123.966
0.410951335	0.324767735	118.671
0.421047503	0.305336343	116.3955
0.455281232	0.319667044	100.3573
0.459	0.3	101.192
0.467847197	0.348148681	88.68375
0.469766964	0.304262441	96.424
0.500680537	0.315956736	87.14785
0.507228745	0.339274498	79.488
0.509	0.3	84.1107
0.51873018	0.303481198	82.36945
0.537476511	0.372411443	72.59025
0.546882986	0.313184492	73.18845
0.54834387	0.332524334	71.9396
0.559	0.3	72.0611
0.567874106	0.302895656	70.56805
0.572084784	0.360638855	63.59595
0.590830771	0.32730311	65.30055
0.593701103	0.311064417	63.6128
0.608835774	0.351290274	58.01025
0.609	0.3	60.59
0.615533102	0.395086552	55.15725
0.617155572	0.302445763	59.9818
0.634413903	0.3232001	56.99725
0.641	0.309409999	55.32005
0.64597291	0.381490544	52.40075
0.647364658	0.343799746	53.4164
0.659	0.3	51.9391
0.666544072	0.302092778	51.92365
0.678734853	0.370285846	49.9497
0.678882169	0.319928212	48.9145
0.687372534	0.337740454	47.12625
0.688680623	0.308096002	47.45725
0.709	0.3	45.3264
0.713499124	0.361016724	44.22885
0.716017458	0.301810822	44.58635
0.72407251	0.317283805	44.39845
0.728615811	0.332791568	43.84745
0.736668854	0.30703612	42.49
0.749987333	0.353310555	41.40665
0.759	0.3	40.0175
0.765559273	0.30158209	38.88855
0.769857779	0.315120208	38.5945
0.770896232	0.328711456	38.753
0.784908275	0.306169475	35.6599
0.787960024	0.346867306	38.2419
0.809	0.3	35.6082
0.81405221	0.325317192	35.11375
0.81515704	0.301394013	34.2332
0.816137856	0.313330165	34.2757
0.82721279	0.341447359	35.7805
0.833355266	0.305452214	32.20075
0.85795163	0.322469323	31.94745
0.859	0.3	32.1705
0.862833124	0.311834096	30.72755
0.864801133	0.301237516	31.1783
0.867571899	0.336859987	30.4036
0.881975623	0.304852153	28.9466
0.902486011	0.32006068	28.16855
0.908889982	0.332953399	28.5581
0.909879662	0.31057213	27.19635
0.947565829	0.318008204	25.52305
0.95104206	0.329606546	25.3544
0.993922029	0.326722556	23.11565

Table A. 5: 3 MeV Electron Eye Lens Dose Table

## APPENDIX D: KERMA vs. Absolute Distance

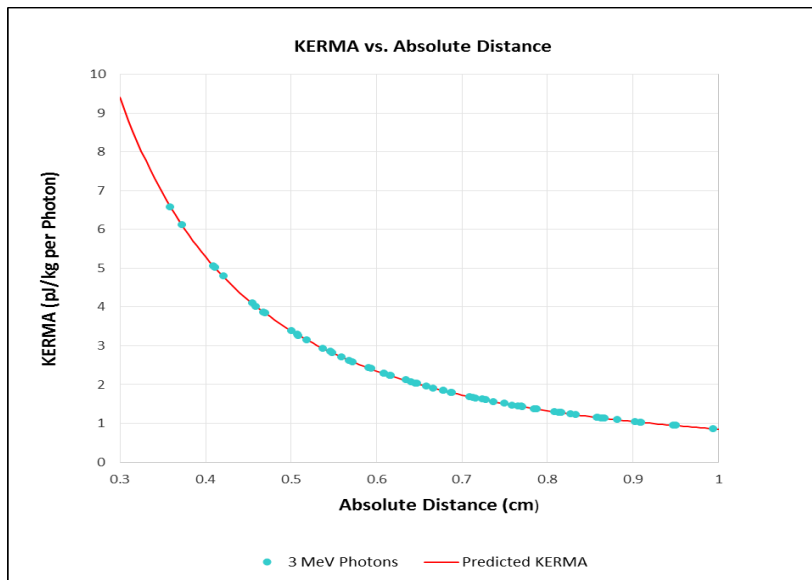


Figure A. 9: KERMA vs. Absolute Distance for 3 MeV Photons

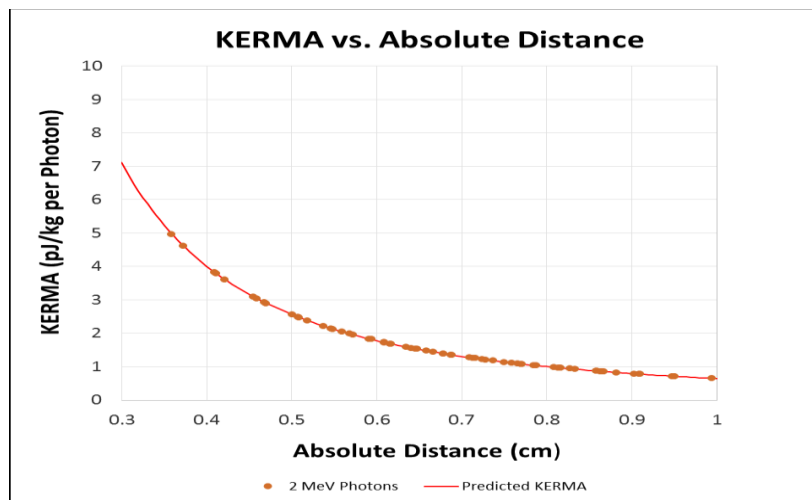


Figure A. 10: KERMA vs. Absolute Distance for 2 MeV Photons

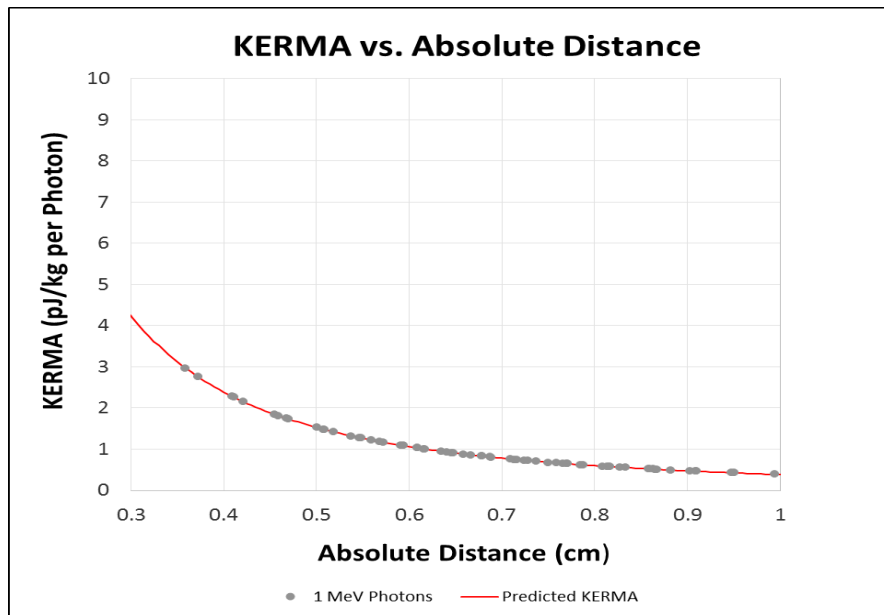


Figure A. 11: KERMA vs. Absolute Distance for 1 MeV Photons

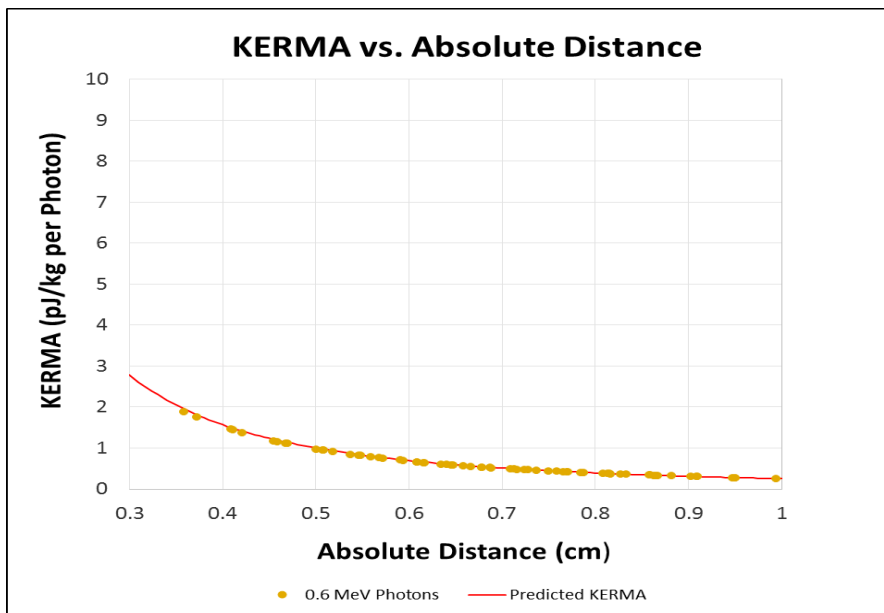


Figure A. 12: KERMA vs. Absolute Distance for 0.6 MeV Photons

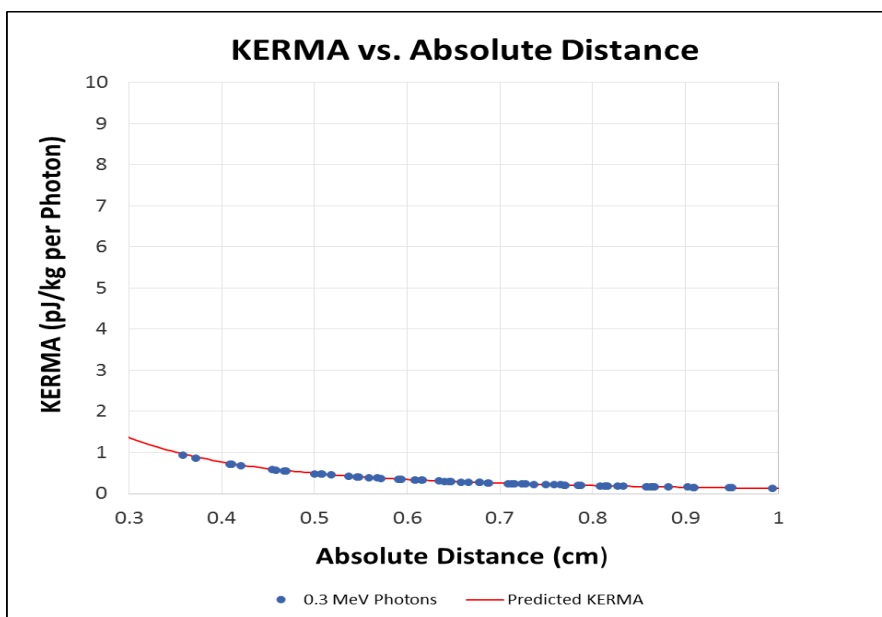


Figure A. 13: KERMA vs. Absolute Distance for 0.3 MeV Photons

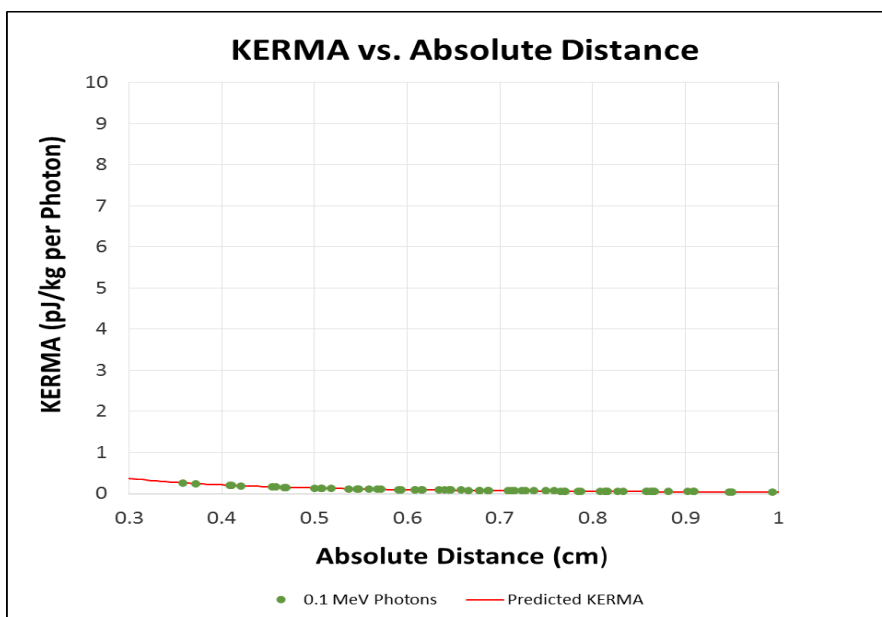


Figure A. 14: KERMA vs. Absolute Distance for 0.1 MeV Photons

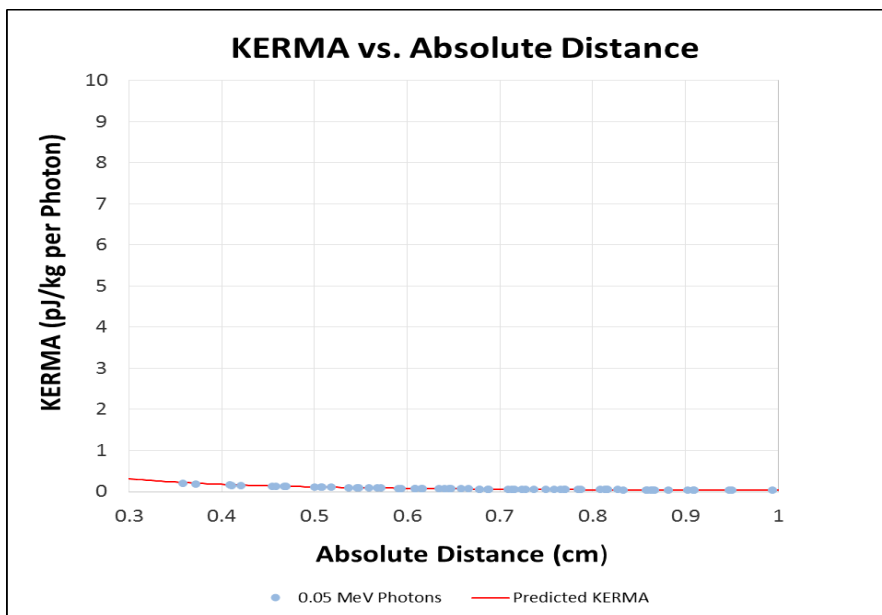


Figure A. 15: KERMA vs. Absolute Distance for 0.05 MeV Photons

## APPENDIX E: MCNP Input File for Electrons

The MCNP6 input file below may be modified to create an input file for each source position and particle type. To change the source position, the input file would need the source definition changed to account for the new x, y, and z components of the source position on line 336. To change the particle type the letter in front of PAR will need to be changed to the desired incident particle such as, e, for electrons or, p, for photons.

2- c Input file of ORNL phantom - Adult male (Eckerman et al., 1996)  
 3- c Cell Cards  
 4- c Detailed model of eye  
 5- C Eyelid  
 6- C  
 7- 301 35 -1.09 (-311 302 -350):(350 -312 323 -351): &  
 8- (351 -312 321 -352):(352 -313 321 -353 317): &  
 9- (353 -313 317 -354):(354 -314 317 315): &  
 10- (354 -314 317 -320) &  
 11- imp:p,e=1 vol 4.23119E+00 trcl 1  
 12- C  
 13- C Sclera  
 14- 302 34 -1.07 (-301 -302 309):(301 -302 303 -350): &  
 15- (350 -355 -323 303):(355 -351 -323 305): &  
 16- (351 -310 305 -321) &  
 17- imp:p,e=1 vol 1.07403E+00 trcl 1  
 18- C  
 19- C Choroid  
 20- 303 34 -1.07 (-301 -309 303) &  
 21- imp:p,e=1 vol 1.73943E-01 trcl 1  
 22- C  
 23- C Retina  
 24- 304 34 -1.07 (-301 -303 305):(301 -303 305 -355) &  
 25- imp:p,e=1 vol 1.81207E-01 trcl 1  
 26- C  
 27- C Cornea  
 28- 305 31 -1.06 -317 319 321 &  
 29- imp:p,e=1 vol 1.09608E-01 trcl 1

30- C  
 31- C Iris  
 32- 306 34 -1.07 -321 322 307 310 &  
 33- imp:p,e=1 vol 2.14913E-01 trcl 1  
 34- C  
 35- C Anterior Chamber  
 36- 300 32 -1.00 -300 imp:p,e=1 vol 3.351032e-5  
 37- 307 32 -1.00 (-319 321):(322 -321 -307 326) #300 &  
 38- imp:p,e=1 vol 1.63431E-01 trcl 1  
 39- C  
 40- C Insensitive volume of Lens  
 41- 308 33 -1.07 -306 -325 -327 &  
 42- imp:p,e=1 vol 1.82558E-01 trcl 1  
 43- C  
 44- C Meridional Rows  
 45- 309 33 -1.07 -318 327 -304 -316 -308 &  
 46- imp:p,e=1 vol 2.03135E-02 trcl 1  
 47- C  
 48- C Germinative Zone  
 49- 310 33 -1.07 -318 324 -326 325 &  
 50- imp:p,e=1 vol 4.19217E-03 trcl 1  
 51- C  
 52- C Transition Zone  
 53- 311 33 -1.07 -318 -324 -327 325 &  
 54- imp:p,e=1 vol 4.64968E-03 trcl 1  
 55- C  
 56- C Central Zone  
 57- 312 33 -1.07 -318 325 326 &

58-                   imp:p,e=1 vol 3.65520E-03 trcl 1  
59-    C  
60-    C Vitreous Humor  
61-    313   32 -1.00 (-305 -310):(310 -322) #308 #309 #310 #311 #312 &  
62-                   imp:p,e=1 vol 4.40078E+00 trcl 1  
63-    C  
64-    C Eyelid  
65-    401    35 -1.09 (-411 402 -450):(450 -412 423 -451): &  
66-                   (451 -412 421 -452):(452 -413 421 -453 417): &  
67-                   (453 -413 417 -454):(454 -413 417 415): &  
68-                   (454 -413 417 -420) &  
69-                   imp:p,e=1 vol 4.23119E+00 trcl 2  
70-    C  
71-    C Sclera  
72-    402    34 -1.07 (-401 -402 409):(401 -402 403 -450): &  
73-                   (450 -455 -423 403):(455 -451 -423 405): &  
74-                   (451 -410 405 -421) &  
75-                   imp:p,e=1 vol 1.07403E+00 trcl 2  
76-    C  
77-    C Choroid  
78-    403    34 -1.07 (-401 -409 403) &  
79-                   imp:p,e=1 vol 1.73943E-01 trcl 2  
80-    C  
81-    C Retina  
82-    404    34 -1.07 (-401 -403 405):(401 -403 405 -455) &  
83-                   imp:p,e=1 vol 1.81207E-01 trcl 2  
84-    C  
85-    C Cornea

86- 405 31 -1.06 -417 419 421 &  
 87- imp:p,e=1 vol 1.09608E-01 trcl 2  
 88- C  
 89- C Iris  
 90- 406 34 -1.07 -421 422 407 410 &  
 91- imp:p,e=1 vol 2.14913E-01 trcl 2  
 92- C  
 93- C Anterior Chamber  
 94- 400 32 -1.00 -400 imp:p,e=1 vol 3.351032e-5 \$ Tally Volume  
 95- 407 32 -1.00 (-419 421):(422 -421 -407 426) #400 &  
 96- imp:p,e=1 vol 1.63431E-01 trcl 2  
 97- C  
 98- C Insensitive volume of Lens  
 99- 408 33 -1.07 -406 -425 -427 &  
 100- imp:p,e=1 vol 1.82558E-01 trcl 2  
 101- C  
 102- C Meridional Rows  
 103- 409 33 -1.07 -418 427 -404 -416 -408 &  
 104- imp:p,e=1 vol 2.03135E-02 trcl 2  
 105- C  
 106- C Germinative Zone  
 107- 410 33 -1.07 -418 424 -426 425 &  
 108- imp:p,e=1 vol 4.19217E-03 trcl 2  
 109- C  
 110- C Transition Zone  
 111- 411 33 -1.07 -418 -424 -427 425 &  
 112- imp:p,e=1 vol 4.64968E-03 trcl 2  
 113- C

114- C Central Zone  
 115- 412 33 -1.07 -418 425 426 &  
 116- imp:p,e=1 vol 3.65520E-03 trcl 2  
 117- C  
 118- C Vitreous Humor  
 119- 413 32 -1.00 (-405 -410):(410 -422) #408 #409 #410 #411 #412 &  
 120- imp:p,e=1 vol 4.40078E+00 trcl 2  
 121- C  
 122- 600 2 -0.00129 #65 -600 601 -602 &  
 123- #301 #302 #303 #304 #305 #306 #300 #307 #308 #309 #310 #311 &  
 124- #312 #313 imp:p,e=1 trcl 1  
 125- C  
 126- 700 2 -0.00129 #65 -600 601 -602 &  
 127- #401 #402 #403 #404 #405 #406 #400 #407 #408 #409 #410 #411 &  
 128- #412 #413 &  
 129- trcl 2 imp:p,e=1  
 130- C  
 131- 65 0 -2:-7:8:-9:10:15 trcl 3 imp:p,e=0 \$ Graveyard  
 132- C  
 133- 5 2 -0.00129 #301 #302 #303 #304 #305 #306 #300 #307 #308 #309 &  
 134- #310 #311 #312 #313 #401 #402 #403 #404 #405 #406 #400 #407 &  
 135- #408 #409 #410 #411 #412 #413 #600 #700 &  
 136- (9 -10 14 22 -12 2 -15 #65):(-22 21 9 -10 2 -15 #65): &  
 137- (-21 2 -6 2 #65):(12 24 -15 9 -10 #65) (2:7:-8:9:-10:-15 #65) &  
 138- imp:p,e=1 trcl 3 \$outsides of phantom  
 139- c  
 140- 6 3 -1.04 ((-23 6 -22 114)):(-21 22 -622 114):((622 -12 -18 116) &  
 141- #41 #43 #17 #301 #302 #313 #303 #304 #306 #401 #402 #403 #404 &

142- #413 #406 #305 #300 #307 #308 #309 #310 #311 #312 #405 &  
 143- #400 #407 #408 &  
 144- #409 #410 #411 #412 #412 #600 #700):((-524 12 116) #43 #42) &  
 145- imp:p,e=1 trcl 3 \$ head and neck  
 146- c  
 147- 7 3 -1.04 (-21 23 6 -22):(22 -622 21 -14):(-14 18 622 -12 #301 &  
 148- #302 #303 &  
 149- #304 #305 #306 #300 #307 #308 #309 #310 #311 #312 #313 #401 &  
 150- #402 #403 &  
 151- #404 #405 #406 #400 #407 #408 #409 #410 #411 #412 #413 #600 &  
 152- #700): &  
 153- (12 -24 524) #600 #700 &  
 154- imp:p,e=1 trcl 3 \$skin  
 155- c  
 156- 17 3 -1.04 -45 &  
 157- imp:p,e=1 trcl 3 \$brain  
 158- c  
 159- 41 5 -1.4 (6 -113 -114) trcl 3 imp:p,e=1 \$spine  
 160- c  
 161- 42 5 -1.4 (-116 45 12 ):(-116 45 -12) &  
 162- imp:p,e=1 trcl 3 \$skull-cranium  
 163- c  
 164- 43 5 -1.4 (118 -117 120 -121 -119 116 #301 #302 &  
 165- #303 #304 #305 #306 #300 #307 #308 #309 &  
 166- #310 #311 #312 #313 #401 #402 #403 #404 #405 #406 #400 #407 &  
 167- #408 #409 #410 #411 #412 #413 ) imp:p,e=1 trcl 3 \$facial skeleton  
 168- c  
 169- c

170- c end of cell Cards  
 171-  
 172- c Surface Cards for Stylized Head Model  
 173- 600 ky -4.5 0.0717967697 1  
 174- 601 py .9  
 175- 602 py 3  
 176- C  
 177- 2 pz 69.0  
 178- 6 pz 70.0  
 179- 7 px -30.0  
 180- 8 px 30.0  
 181- 9 py -30.0  
 182- 10 py 15.0  
 183- 12 pz 91.45  
 184- 14 sq 100 64 0 0 0 0 -6400 0 0 0 \$head1-skin  
 185- 15 pz 100.0  
 186- 18 sq 96.04 60.84 0 0 0 0 -5843.0736 0 0 0 \$head1  
 187- 21 cz 5.4  
 188- 22 pz 78.40  
 189- 622 pz 78.6  
 190- 23 cz 5.20 \$neck  
 191- 24 sq 5112.25 3271.84 6400 0 0 0 -327184 0 0 91.45 \$head2  
 192- 524 sq 4638.172 2938.72 5843.074 0 0 0 -282235.1 0 0 91.45 \$head2  
 193- 45 sq 2445.3025 1440.2025 3221.6976 0 0 0 -106517.3769 0 0 91.45 \$brain  
 194- c 37 pz 43.0  
 195- 113 pz 84.8  
 196- 114 sq 6.25 4 0 0 0 0 -25 0 1.45 0 \$ spine-upper

197- c 45 sq 2445.3025 1440.2025 3221.6976 0 0 0 -106517.3769 0 0 91.45  
 \$skull -crni  
 198- 116 sq 3991.080625 2487.515625 5076.5625 0 0 0 -224498.28515625 0 0  
 91.45 \$skull  
 199- 117 sq 81 49 0 0 0 0 -3969 0 0 0 \$ facial skeleton  
 200- 118 sq 57.76 31.36 0 0 0 0 -1811.3536 0 0 0 \$facial skeleton  
 201- c 80 sq 5112.25 3271.84 6400 0 0 0 -327184 0 0 91.45 \$the statements  
 defining th  
 202- 119 py 0.0  
 203- 120 pz 82.4  
 204- 121 pz 93.13  
 205- C  
 206- c Surface Cards for Stylized Eye Model  
 207- C Tally Locations  
 208- 300 S -3 -0.941 0 0.02  
 209- 400 S 3 -0.941 0 0.02  
 210- C Eye Surfaces  
 211- 301 PY .024  
 212- 302 SO 1.174  
 213- 303 SY 0.048 1.074  
 214- 304 SY 0.759 0.5  
 215- 305 SY 0.098 1.074  
 216- 306 SY 1.291 0.8  
 217- 307 CY 0.15  
 218- 308 SY 1.0364012305223 0.6  
 219- 309 SO 1.074  
 220- 310 PY 0.42022  
 221- 311 SO 1.399  
 222- 312 SY 0.08 1.399

223-	313	SY	-0.38	1.575			
224-	314	SY	0.466	1			
225-	315	P	0	-5.87	8.09	-2.18462	
226-	316	SY	0.433747228596	0.595			
227-	317	SY	0.466	0.775			
228-	318	SY	-0.339	1.25			
229-	319	SY	0.466	0.72			
230-	320	P	0	4.226	14.463	-2.75194	
231-	321	SY	-0.38	1.35			
232-	322	SY	-0.38	1.3			
233-	323	SY	0.08	1.174			
234-	324	PY	0.85				
235-	325	SY	-0.359	1.25			
236-	326	PY	0.8775				
237-	327	SY	0.759	0.45			
238-	350	PY	0.04				
239-	351	PY	0.33285				
240-	352	PY	0.418939130435			\$ Intersection of 12 and 13	
241-	353	PY	0.76515				
242-	354	PY	0.918073877068558				
243-	355	PY	0.073				
244-	C						
245-	401	PY	.024				
246-	402	SO	1.174				
247-	403	SY	0.048	1.074			
248-	404	SY	0.759	0.5			
249-	405	SY	0.098	1.074			
250-	406	SY	1.291	0.8			

251-	407	CY	0.15				
252-	408	SY	1.0364012305223	0.6			
253-	409	SO	1.074				
254-	410	PY	0.42022				
255-	411	SO	1.399				
256-	412	SY	0.08	1.399			
257-	413	SY	-0.38	1.575			
258-	414	SY	0.466	1			
259-	415	P	0	-5.87	8.09	-2.18462	
260-	416	SY	0.433747228596	0.595			
261-	417	SY	0.466	0.775			
262-	418	SY	-0.339	1.25			
263-	419	SY	0.466	0.72			
264-	420	P	0	4.226	14.463	-2.75194	
265-	421	SY	-0.38	1.35			
266-	422	SY	-0.38	1.3			
267-	423	SY	0.08	1.174			
268-	424	PY	0.85				
269-	425	SY	-0.359	1.25			
270-	426	PY	0.8775				
271-	427	SY	0.759	0.45			
272-	450	PY	0.04				
273-	451	PY	0.33285				
274-	452	PY	0.418939130435	\$ Intersection of 12 and 13			
275-	453	PY	0.76515				
276-	454	PY	0.918073877068558				
277-	455	PY	0.073				
278-	c end surface cards						

279-  
 280- c Translation to put eye in correct place  
 281- tr1 -3 0 0 1 0 0 0 -1 0 0 0 1  
 282- tr2 3 0 0 1 0 0 0 -1 0 0 0 1  
 283- tr3 0 8 -85.5 1 0 0 0 1 0 0 0 1  
 284- c Material Cards  
 285- m2 7000 0.8 8000 0.2 \$air  
 286- m3 1000 10.454E-02 6000 22.663E-02 7000 2.490E-02 8000 &  
 287- 63.525E-02 11000 0.112E-02 12000 0.013E-02 14000 0.030E-02 &  
 288- 15000 0.134E-02 16000 0.204E-02 17000 0.133E-02 19000 &  
 289- 0.208E-02 20000 0.024E-02 26000 0.005E-02 30000 0.003E-02 &  
 290- 37000 0.001E-02 40000 0.001E-02 \$soft tissue  
 291- m5 1000 7.337E-02 6000 25.475E-02 7000 3.057E-02 8000 &  
 292- 47.893E-02 9000 0.025E-02 11000 0.326E-02 12000 0.112E-02 14000  
 0.002E-02 &  
 293- 15000 5.095E-02 16000 0.173E-02 17000 0.143E-02 19000 &  
 294- 0.153E-02 20000 10.190E-02 26000 0.008E-02 30000 0.005E-02 &  
 295- 37000 0.002E-02 38000 0.003E-02 82000 0.001E-02 \$skeleton  
 296- C Cornea, den=1.06  
 297- m31 1000 -10.3 \$ Hydrogen  
 298- 6000 -10.9 \$ Carbon  
 299- 7000 -03.5 \$ Nitrogen  
 300- 8000 -75.1 \$ Oxygen  
 301- 16000 -00.2 \$ Sulfur  
 302- C  
 303- C Anterior Chamber, Vitreous Humour, den=1.00  
 304- m32 1000 -11.2 \$ Hydrogen  
 305- 8000 -88.8 \$ Oxygen

306- C  
307- C Lens, den=1.07  
308- m33 1000 -09.06 \$ Hydrogen  
309- 6000 -19.5 \$ Carbon  
310- 7000 -05.7 \$ Nitrogen  
311- 8000 -64.6 \$ Oxygen  
312- 11000 -00.1 \$ Sodium  
313- 15000 -00.1 \$ Phosphorous  
314- 16000 -00.3 \$ Sulfur  
315- 17000 -00.1 \$ Chlorine  
316- C  
317- C Retina, Choroid, Sclera den=1.07  
318- m34 1000 -10.0 \$ Hydrogen  
319- 6000 -14.6 \$ Carbon  
320- 7000 -04.5 \$ Nitrogen  
321- 8000 -70.6 \$ Oxygen  
322- 16000 -00.3 \$ Sulfur  
323- C  
324- C Eye Lid, den=1.09  
325- m35 1000 -10.0 \$ Hydrogen  
326- 6000 -19.9 \$ Carbon  
327- 7000 -00.42 \$ Nitrogen  
328- 8000 -65.0 \$ Oxygen  
329- 11000 -00.2 \$ Sodium  
330- 15000 -00.1 \$ Phosphorous  
331- 16000 -00.2 \$ Sulfur  
332- 17000 -00.3 \$ Chlorine  
333- 19000 -00.1 \$ Potassium

334- mode p e  
335- c Source Cards  
336- sdef par e erg 3 pos 2.5 -1.3 0 vec 0.5 0.359 0 dir D1  
337- SI1 -1 0.965925826289068 1  
338- SP1 0 0.982962913144534 1.70370868554658E-02  
339- SB1 0 0 1  
340- c Tally Cards  
341- +F6 400 300  
342- FM6 1.60218E-10  
343- mplot tal 6 free f freq 10000 plinear linlin  
344- c PRDMP 10000  
345- STOP F6 0.025 CTME 600